Hydraulic Properties Characterization of 3D Printed Sandstone Analogues

by

Nathalia Andrea Ardila Angulo

A thesis submitted in partial fulfillment of the requirements for the degree of

Master of Science

in

Geotechnical Engineering

Civil and Environmental Engineering
University of Alberta

Abstract

Accurate modeling of production performance and recovery processes in petroleum and gas reservoirs is heavily influenced by the heterogeneity of natural geomaterials. Reliability of these studies regarding accurate estimation of the hydraulic properties of the reservoir rock stratum constitutes a challenging condition to be handled by the implementation of additive manufacturing (AM) technology. This fabrication technique is intended to provide a valuable tool not only for assuring heterogeneity and repeatability within the built specimens, but also to recreate specific properties of the reservoir rock and provide, in a foreseeable future, a suitable means to validate numerical models related to geomechanical in-situ processes. Therefore, for the purposes of emulating petrophysical and flux properties of a specific reservoir rock, it is imperative to recognize features arising from the AM process and their impact on printed specimens. By means of this project, a complete comprehensive analysis of the influence of printing configuration was accomplished to determine whether these variables influence the resulting hydraulic properties of the sandstone analogues. A complete range of petrophysical testing analyses were performed to evaluate the potential of 3D printed sandstone analogues to be a state-of-the art material at simulating the behavior of materials found in nature. Testing results demonstrate that additive manufacturing technology can be successfully used to generate sandstone replicas with properties and structure of the printed specimens interrelated with the properties of natural materials. However, some discrepancies on the range of values encountered for 3D printed materials

compared with the properties of natural reservoir rocks remain. For instance, a direct comparison between common hydraulic values of Berea sandstone and manufactured materials has shown an increase of 41.6% on permeability values and of 44.3% on porosity for the 3D printed analogues.

Keywords: Additive Manufacturing Technology, 3D Printing, Sandstone analogues, Hydraulic and Petrophysical Properties.

Dedication

To God, who gave me strength in times when there seemed to be no way out, in whom I was able to secretly trust all my joys and worries.

To my parents, who accompanied, advised and gave me their example of hard work, deep love and strength during all the stages of this proces.

To Sebastian, who has offered unwaveing support and encouragement since we have been together. Also for his love and sacrifices

To my sisters and my nephews who always gave me the best of themselves. Their love and company made this experience much more valuable.

Because they are the wind beneath my wings.

Acknowledgement

The author gratefully acknowledges to Dr. Chalaturnyk and Dr. Zambrano for their priceless technical support. Also, she thanks the financial support of the Foundation CMG Industrial Research Consortia to the Reservoir Geomechanics Research Group [RG^2] at the University of Alberta. A special recognition also goes to the staff from Geo-REF facilities that contributed with her experience and knowledge to this work.

Table of Contents

Table of Figures

Table of Tables

CHAPTER 1 INTRODUCTION

1.1 Statement of the problem

Natural rocks are certainly heterogeneous; the particles that compose sedimentary rocks undergo different physical and chemical alteration processes during transportation, deposition, burial and subsequent diagenesis periods within the Earth's crust. These conditions generate a distinctive and unrepeatable set of physical properties that cannot be encountered in any other sample. Even though, occasionally the bulk properties of two rocks can be similar between each other, certain differences in rock fabric or microstructure might exist. Consequently, petrophysical (i.e. porosity, wettability, permeability) properties' measurement performed on natural sandstones corresponds to a single point-in-time-and-space, a specific stage of the diagenetic process of each individual rock (Head and Vanorio 2016). Therefore, when the collected experimental data is merged together, it seems to have a non-specific trend (Lucia 1995), so theoretical generalizations must be included to truly capture the practical relationship between the parameters analyzed in a particular study and in that way, validate the numerical models built for any specific geomechanical application.

The possibility of 1) isolating experimental results from the natural heterogeneity induced by sedimentation and lithification processes, 2) the capability of controlling specific crucial aspects on sedimentary rocks as grain size and its distribution, density distribution, amount and type of cementing material, porosity and even fracture networks and 3) the opportunity to test the material response independent from pore-structure variability are some of the now-available options facilitated by 3D printing technology. By knowing this, 3D printing of geomaterials arises as a valuable resource to assess the degree of influence of pore geometry and structural heterogeneity on rocks' macroscopic flow properties.

However, it is imperative the recognition of whether this technology, 3D printing, will serve as a mechanism to replicate the behavior of those materials found in the nature (i.e. natural rocks). Therefore the study and characterization of this material must be addressed. The starting point is to characterize hydraulic and petrophysical properties of 3D printed sandstone analogues. Hence, to fully understand the hydraulic behavior of the printed samples, to analyze the influence of the printing process on their petrophysical and flow properties; and to determine whether they mimic

natural porous media and serve as a defensible material to recreate any geomechanical process on reservoir sandstones; a series of permeability, porosity, wettability, compressibility and mercury injection tests were performed on different specimens. Moreover, to understand the incidence of the printing parameters in the petrophysical properties of the samples, the cylinders used for the testing campaign were fabricated using different printing configurations.

1.2 Research Objectives

Over the last decade the additive manufacturing industry has rapidly grown resulting in the commercial availability of a wide range of 3D printing machines based on various printing technologies and printing materials. The usage of these materials in the geomechanical industry depends not only upon the understanding of their behavior when subjected to external alterations, but also the knowledge of their intrinsic properties. Therefore the characterization of fundamental flow and petrophysical properties of 3D printed sandstone analogues is the main objective of this research program. This investigation will cover the characterization of properties such as, porosity, wettability and permeability. Moreover this study will provide a sufficient insight on the impact of specimen print configurations on sample's anisotropy and flow properties. Finally, the results obtained by the testing campaign will be compared with those existing from the literature for natural sandstones such as Berea and Fontainebleau sand formations.

1.3 Scope and Methodology

The accurate modeling of production performance and recovery processes in petroleum and gas reservoirs is heavily influenced by the heterogeneity of natural geomaterials. The reliability of these studies on the accurate estimation of the hydraulic properties of the reservoir rock stratum constitutes a challenging condition to be handled by the implementation of additive manufacturing processes. 3D printing techniques will provide to the researchers the ability of ensuring the repeatability of petrophysical and flux properties determined by experimental processes in laboratory. The scope of this research includes a complete comprehensive analysis of the influence of printing configuration and features to determine whether, and in which manner, these variables influence the resulting hydraulic properties of the rock analogues to be fabricated. To achieve the research objective, the testing campaign for the entire tests will be performed as follows:

1. Build up the test-samples with the different variations of printing configurations that are intended to be analyzed, assuring that at least three specimens with equivalent properties (i.e. built using the same set of printing features) are included in the testing population to analyze repeatability of the results.
2. Run the testing campaign maintaining constant the test and boundary conditions so that the results can be compared and analyzed avoiding the influence of external factors.

1.4 Organization of Thesis

The overview of additive manufacturing technology is presented in Chapter two. It describes the development of the 3D printing industry in recent years. It also lists the printing process of the ExOne M-Flex^{TM} 3D Printing and the materials and binders that are used to build the specimens.

Chapter three explains the main variables that are studied to analyze the influence of printing configuration on the hydraulic properties of the 3D printed specimens. Binder saturation, layer orientation and layer thickness of the samples are the main parameters examined for this research.

Uniaxial confining stress (UCS) and permeability test are presented in Chapter four. UCS tests were performed to determine how the mechanical behavior of the specimens were affected by exposure to different fluids. The test facility and experimental results for the permeability test based on various printing configurations are also described in this chapter.

Chapter five focuses on the preference of the fluid to spread on or adhere to the solid surface of the 3D printed specimens. Contact angle measurements and both co-current and counter-current imbibition tests were performed to determine the wettability of this material.

Mercury intrusion capillary pressure tests were performed on cylinders created by varying the printing configurations. Pore size distribution, porosity and average pore diameter results are presented in Chapter six.

Chapter seven presents the conclusions and recommendations for future research.

2 CHAPTER 2 ADDITIVE MANUFACTUING TECHNOLOGY

2.1 Introduction

Continuous technological advancements have allowed the creation of three-dimensional objects using inkjet technology. This revolutionary method for creating 3D models, also known as Additive Manufacturing Technology (AM), saves time and cost by eliminating the need to design, print, and glue together separate model parts. The development of this technology has resulted in a wide range and prototypes of commercial 3D printer models with the usage of different printing materials. Each model has its specific application in different industries depending on the material and resolution of the machine. Currently, the vast majority of 3D printers utilize plastic to build up the desired shape or geometry, however; printers that employ metals, ceramics, cements or sand as the building material are already available in the market.

The evaluation of printing with different materials must be addressed with the purpose of using these new resources in different industries. For instance, in the rock mechanics world, the possibilities of 3D printing have been recognized. However, all research advances are based on specimens printed with plastic. The opportunity to generate three-dimensional objects using granular materials will give us the chance to study a more realistic material with the advantage of switching different parameters that cannot be controlled in natural rocks. Some examples of these parameters are the amount and type of cementing material, the grain size distribution and the geometry and position of discontinuities among others.

2.2 3D Printing Technologies

Additive manufacturing (AM) is an emerging technology that is gaining traction among the manufacturing industries. The process of generating a new object with this technology starts with a 3D model of the piece, which commonly is created using computer-aided design (CAD) software. The AM machine then creates the object by forming each layer via the selective placement of material. There are several AM processes that are distinguished from each other by the way in which they build each layer. The techniques for creating each step ranges from jetting a binder into a powder, using a UV laser to harden a photosensitive polymer, to using laser to

selectively melt metal or polymeric powder. Additionally, a great number of materials can be used simultaneously to create a mixed material capable to meet the client requirements. Complex geometries can be also printed offering a geometrical freedom in engineering design (Campbell et al. 2011). At the same time it offers well-designed and useful objects without the need for assembly, saving production time and money.

The rapid development of the 3D printing industry has resulted in the commercial availability of a wide range of 3D printer models (Osinga, et al 2015), all with different applications. Most widely used in applications with low production volumes, small part sizes, and having complex designs (Berman 2012).The most revolutionary developments in AM technology with its applications are listed below with the purpose of summarize and contextualize the reader with the advancements in the 3D printer technology.

Biomaterials and Medical Applications

There are many potential uses for 3D printing in medicine that it is expected this technology will revolutionize healthcare with the fabrication of different biomaterials (Schubert et Al. 2014). A number of recent reviews have been published with a promising future for 3D printing technology in the medicine world. Both, actual and potential usages can be categorized into numerous groups, such as, tissue and organ fabrication; creations of customized prosthetics; implants and anatomical models; and pharmaceutical research regarding drug dosage forms, delivery, and discovery (Ventola 2014).

More specific applications and studies are (1) 3D printing of layered brain-like structures consisting of discrete layers of primary neural cells encapsulated in hydrogels. These structures offers the chance to reproduce more accurate 3D in vitro microstructures with benefits varying from cell behavior studies to refining the understanding of brain injuries and neurodegenerative diseases (Lozano et al. 2015). (2) Tissue or organ failure is another critical medical problem that can be overcome with the usage of AM technology. 3D bio-printing offers the advantage of producing cells and biomaterials which are created layer by layer forming a tissue-like structure which at the end form the shape of the organ (Ozbolat and Yu 2013). The procedure of organ printing as well as other 3D printing technologies can be subdivided into three sequential steps: 1) Preprocessing which is the development of a computer-aided design which is mostly derived

from digitized image reconstruction of a natural organ or tissue; 2) Processing, it refers to the layer-by-layer placement of cells into a 3D environment using the CAD file previously uploaded; and 3) the post-processing part involves the perfusion of printed organs and their biomechanical conditioning to both direct and accelerate organ maturation (Mironov et al. 2003). The creation of bone tissue, among the different technology options, is another opportunity to utilize 3D printing equipment with the purpose of enhancing the life and health. This technology allows the printing of porous scaffolds with any designed shape with the ability of controlling chemistry and interconnected porosity. Some of these inorganic scaffolds are biodegradable and have proven ideal for bone tissue engineering (Bose et al. 2013).

Another important benefit offered by 3D printing is the ability to produce items such as prostheses and surgical instruments that can facilitate the development of the health care sector. The capability of rapidly create personalized prostheses solves a frequent problem in orthopaedics, where standard implants are not often satisfactory for great part of the patients. Additionally, productivity is increasing in terms of the number of cubic centimeters you can build in an hour, and there is also better resolution, accuracy, reliability, and repeatability (Banks 2013). On the other hand, investigations have concluded that a cost per unit of a 3D-printed reactor for the manufacturing of surgical instruments is one 10^{th} the cost of a stainless instrument, with the capability of producing sterile ready-to-use instruments (Rankin et al. 2014).

Casting Applications

Metal casting are universally used for industrial, military and consumer products and are increasingly being evaluated for cost-effective applications in new product development programs. AM technology applied in metal casting has given the manufacturers the ability to produce aluminum and other non-ferrous casting at high speed and low cost. Most of the 3D printer models utilize different casting methods in their processes, such as 1) the direct pour and shell method which involves the generation of molds which after drying, the user casts metal directly into the 3D printed mold set and 2) production intent casting, which involves the direct creation of cast metal tools from CAD data in a cost-effective manner (Bak 2003).

Studies (Bassoli et al. 2007) have shown that using 3D printing for metal casting offers satisfactory results providing a much higher geometrical freedom. Additionally it offers a solution for effective

production of cast technological prototypes, in very short times, avoiding any tooling phase and with dimensional tolerance that are completely consistent with metal casting processes.

ExOne, a manufacturing technology company, presented a list of case studies from all segments of industry where 3D printing has play an important role in the enhancement of the fabrication of metal parts. These case studies list a variety of solutions such as, the production of pump impellers, small runs, personalized bicycles, complex automotive prototypes, metallic parts used in mining, working hand tools, standard alloys, tail cones for submarines, rotors and stators for down hole applications, among others (3D Printing Materials | ExOne n.d.). Materials used in metal casting ranges from different kinds of stainless steel to ceramic beds, alloys, iron, aluminum, chromite, zircon and tungsten.

Soil Biology and Biochemistry

Measurements of the soil have allowed a better understanding of the soil architecture. However there is no an experimental technique to reproduce the complexity in microcosms. X-ray CT imaging in conjunction with 3D printing allow the creation of microcosms replicas exhibiting the physical heterogeneity found in soils. These printing materials are suitable to study the fungal growth, the physical heterogeneity on fungal spread and the role of transport processes. This technology is argued to open up a wealth of opportunities for soil biological studies (Otten et al. 2012).

Additive Manufacturing with Plastics

The enormous majority of 3D printers produce plastic parts. Nylon and polyamide are the most common type of polymers used in the fabrication of 3D printed objects. They are strong, flexible and durable. Also, they are naturally white in color; therefore the plastic can be painted with any color combination. Other plastics used in the manufacturing of 3D items are the acrylonitrile butadiene styrene (ABS) and polylactic acid (PLA), the last material being a biodegradable thermoplastic derived from renewable resources. Polyvinyl alcohol (PVA) is a plastic that is water-soluble; this material is often used to provide a support structure to objects with overhang issues. All the different plastics used for the development of numerous objects, allow the development of different designs and applications for any industry

Finally, some of the more remarkable advantages of 3D printing in comparison to other technologies are the ability of recycle waste material; automated manufacturing; no requirements for scrap, milling and sanding; no need for costly tools, molds or punches; the ability to easily share designs and outsource engineering; it speed up the designing and modifying of the objects; and the cost effective manufacturing of the products. Nonetheless, as AM is a new emerging technology there are still some limitations, such as a reduced choice of materials or the limited strength of the finished object, that must be overcome with time.

2.2.1 3D printing in rock mechanics and hydraulic disciplines

Although the prospects of generating specimens with a 3D printer for the study of its mechanical and hydraulic properties have been recognized, plastic has been the prevalent material of choice. Head and Vanorio (2016), for example, investigated the flow properties of 3D printed specimens using photo-reactive resin. The study concluded that the 3-D printing methodology helps improve experimental repeatability by allowing duplication and the opportunity to access and connect multiple scales digitally and experimentally. However, the technique is limited to applications with larger, simple pore geometries, which are certainly not representative of all natural samples. Powder-based inkjet 3D printing method was utilized with the purpose of generating solutions to many of the problems encountered with natural materials and with specimens printed with substances that are far away from the natural behavior of the rocks. Several authors (Fereshtenejad and Song 2016 and Farzadi et al. 2014) investigated the mechanical behavior of powder-based 3D printed cylinders. It was concluded that these specimens behave similarly to those of natural rocks but with lower strength. Additionally, they also assert that further improvements are required to expand 3D printing technology in the area of rock mechanics. For this reason, sand was selected as the printing material to be studied in the present project. It is expected that printing with sand will enhance the behavior of the material generated after the printing process, creating a material more like those found in the nature. Moreover, the hydraulic characterization of the specimens will provide a better understanding of this material.

2.3 ExOne M-Flex™ 3D Printer

The specimens utilized in the present study were manufactured using the M-Flex™ 3-D printer system designed by ExOne. The system was acquired and installed in the GeoPRINT facility at the University of Alberta by the Reservoir Geomechanics Research Group (RG2), as part of a Foundation CMG Industrial Research Consortia in Reservoir Geomechanics. This 3D printer machine has a build total volume of 400 x 250 x 250 mm and a print resolution of 63.5 μm, 60 μm and 100 μm in the X, Y and Z directions, respectively (ExOne User Manual, 2014).
The machine has five main doors, allowing access to 1) the print head system, 2) the fluid and pneumatic cabinet, 3) the job box, 4) the work area, and 5) the recoater. The schematic and the description of each section are presented in Figure 2.1 and in Table 2.1.

Table 2.1 Description of Each Access Point

Name	Function
1. Print Head System	
1.1 Y-Axis Motor	Moves the print head in the Y direction.
1.2 Print Head	1024 jet drop on demand print head. Deposits binder onto the print bed to form a print.
1.3 Capping Station	Resting area for the print head when not in use. Maintains humidity at the print head jets.
1.4 Test Print Area	Holds thermal paper for test prints as well as felt pads for drop mass tests.
1.5 Wiper and Wiper Trough	Cleans the print head periodically during idle cleaning, cleaning, and printing.
1.6 Priming Area	Area for binder to drain while priming the print head, gives access for manual cleaning of the print head if necessary.
2. Fluid and Pneumatic Cabinet	
2.1 Binder Reservoir	Contains binder for printing, must be filled before printing.

2.2 Cleaner Reservoir	Contains cleaner for cleaning the print head, must be filled before printing.
2.3 Water Reservoir	Contains a mixture of binder and waste for disposal, must be emptied before printing.
2.4 Cleaner Filter	Filters cleaner for pumping into the wiper trough and capping station.
2.5 System Compressed Air Regulator	Regulates air pressure to the system components.
2.6 Actuator Valve Manifold	Directs high pressure air to various system components.
2.7 Print Head Compressed Air Regulator	Provides compressed air supply to the print head for priming.
2.8 Pump Enclosure Assembly	Houses all pump motors.
2.9 Vacuum Ballast	Prevents spikes or drops in vacuum pressure in the print head systems.
2.10 Binder Filter	Filters binder before pumping into the print head reservoir.
3. Job Box and Z-Axis Access	
3.1 Job Box	Contains the powder bed and printed parts for transfer into curing oven and de-powdering station.
3.2 Job Box Retaining Latch and Handle	Holds the job box in place when inserted.
3.3 Powder Drip Tray	Drip tray for powder pushed through the job box seal
3.4 Z Axis Bottom end stop sensor	Low-limit sensor for the Z Axis
3.5 Z Axis	Engages the print bed. Includes the platen, platen magnets, and alignment shafts.
3.6 Z Axis Motor	Raises and lowers the print bed. 1.0 micron accuracy.
4. Work Area	

4.1 Recoater Assembly	Deposits a precise layer of powder onto the print bed.
4.2 Job Box	Contains the powder bed and printed parts for transfer into curing oven and de-powdering station.
4.3 X-2 Axis	Moves the recoater/heater carriage in the X direction.
4.4 X-1 Axis	Moves print head carriage in the X direction
4.5 Recoater Powder Level Sensor	Senses the powder level in the recoater, prompts a refill command when low
4.6 Thermal Sensor	Senses the temperature of the print bed for automatic bed temperature control
4.7 Exhaust Fans	4" brushless fans, may be connected to facility exhaust.
5. Recoater Access	
5.1 X-1 Axis Motor	Moves the X1 Axis, which contains the print head assembly.
5.2 Recoater Slot	Slot from which powder is deposited during recoating.
5.3 Heater Assembly	Heats the print bed to prepare for recoating.
5.4 X-2 Axis Motor	Moves the X2 Axis, which contains the recoater assembly.
5.5 Front Low Powder Level Sensor	1 of 2 sensors that detect low powder level, resulting in a warning to add powder.
5.6 Powder Hopper	Holds powder to be deposited into the recoater.
5.7 High Powder Level Sensor	Sensor that detects high-level powder (for use with powder loader only)
5.8 Rear Low Powder Level Sensor	1 of 2 sensors that detect low powder level, resulting in a warning to add powder.

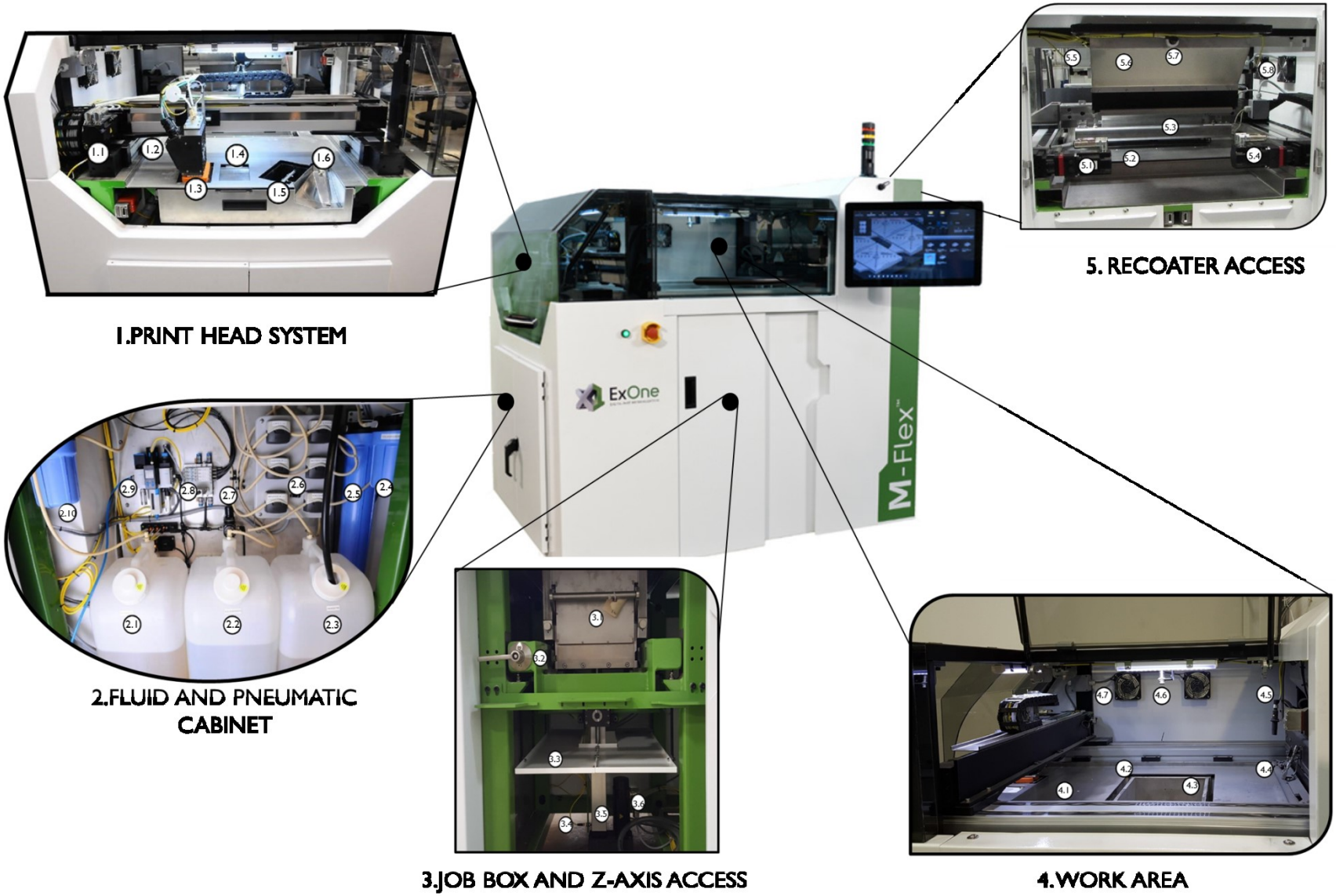

Figure 2.1 M-Flex 3D Printer System Schematic

2.3.1 Materials

Silica sand is universally known as one of the most frequent and simple varieties of sand. It is derived from quartz that over time, as a result of the work of different transport mediums, has been fragmented into minuscule granules. It is used for a wide range of applications; for instance, in oil and gas industry is used in large quantities as proppant in hydraulic fracturing operations. It is also used for construction engineering and for fabrication of parts in glass, ceramics and chemical industries, among others. With the advances in additive manufacturing technologies, another application for silica sand has been found: the creation of natural rock analogues is now possible using a mixture of this material and a binding liquid.

With the purpose of assessing the particle size distribution of this granular material, a sieve analysis was performed (Particle Size Distribution. M-Flex Sand 2015). Results are presented in Figure 2.2, suggesting a well-sorted granular material with a particle diameter representing the 50% cumulative percentile value (D_{50}) of 175 μm.

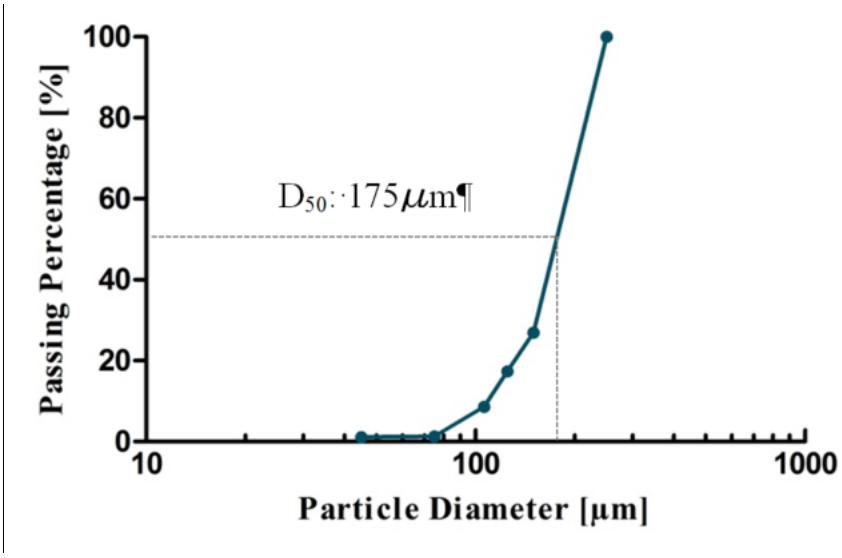

Figure 2.2 Particle Size Distribution of Silica Sand

2.3.2 Binders

The selection of the binder is one important aspect that has to be properly addressed, as it will serve as the cement between particles. Its selection depends upon the type of powder and the system (i.e. model and specification of the printer) that is being used. ExOne® Binders offers four different binding materials, furan binder, phenolic binder, silicate binder and aqueous-Based binder. The most suitable binder to be used with silica sand is Furan binder, which was the fluid selected as the cement material in this research. The trade name is FB001 Furan Binder and some of its physical and chemical properties are stated in Table 2.2 (ExOne 2009). It is mainly composed by furfuryl alcohol (70 to 90%). Other components are bisphenol A (5-15%), resorcinol (1-10%) and 3-aminopropyltriethoxysilane (0.1-0.2%).

Table 2.2 Physical and Chemical Properties of FB001 Furan Binder

Appearance	
Form	Fluid
Color	Brown
PH- Value at 20 C	6-8
Boiling Point	170 C (Furfylalkohol
Flash Point	65 – 80 C
Ignition Temperature	390 C

Furfuryl alcohol and furan resins are a group of polymeric liquids derived from compounds containing the basic furan ring structure. They can be resinified with a conventional acid catalysis and cured to provide infusible solid products (Schmitt 1974). To generate the exothermic reaction that will lead into the polymerization of the furan binder, an acidic activator has to be previously mixed with the sand. FA001 Activator is used in the production of casting molds and cores, also as a hardening and curing agent. It is mainly composed by p-toluenesulphonic acid, containing a maximum of 5% H@SO4. It is a brown fluid with a pH-value below 1, its boiling point is 100 C and the flash point is above 100C.

2.4 3D Printing Process

In order to manufacture the samples, the M-Flex^{TM} uses a layered deposition and binding process that involves three major phases: first, the silica sand, which was selected as manufacturing material because of its inherent similarities with the mechanical properties of natural sandstones, is pre-coated with an acid activator (Sulfonic Acid), later used as a catalyst for the polymerization reaction of the furan binder into resin inside the sample's pore structure. Second, a thin layer of the pre-coated silica sand is deposited onto the building platform. Right after, the printing head passes over the printing bed selectively depositing a pre-set volume of furan binder into the silica sand layer, replicating the specimen's shape. When this progression has been completed, heat is applied to the recently bound layer to enhance crystallization of the resin. With each successive coating of the print head, a new layer is bound until a near-net shape object is completed (Osinga et al, 2015). Finally, the samples are placed inside an oven with the purpose of completing furan binder's curing process.

2.5 Thermal Treatment to Cure the Specimens

Primkulov et al., 2017, stated that over a range of temperatures (from ambient conditions up to 200°C), the optimum temperature to avoid ring hydrolysis of the monomers is 80°C, which can result in a considerably reduction of the mechanical properties of the specimens. Standard practice developed within the personnel involved on the research project, established a minimum of 12 hours of high-temperature curing to ensure fully completion of the process. This was also confirmed by Primkulov et al., 2017 who observed a plateau on the peak strength vs. curing time's relationship for specimens cured for minimum of 1.5 hours as shown in Figure 2.3.

The curing map for furfuryl alcohol binder, as shown in Figure 2.3, within printed specimens is showing a temporal evolution of peak strength of samples cured at 25°C, 60°C, 80°C 115°C, 150°C and 200°C. The black line represents the sample strength evolution with time at 80°C. The reaction of the furfuryl acetate with the acid turns the specimens in a deep green color (McKillip William 1989). However, when the curing process is over (when reaching the black line in Figure 2.3), the color of the specimens becomes even darker due to the crystallization of the polymer.

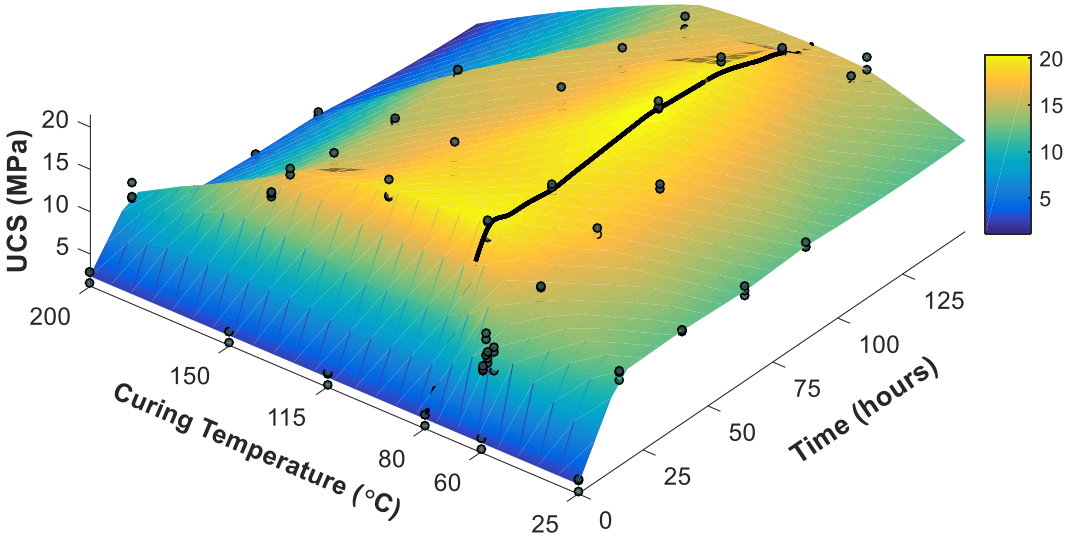

Figure 2.3 Evolution of peak strengths of samples cured at different temperatures (after Bauyrzhan Primkulov* 2017)

3 CHAPTER 3: PRINTING CONFIGURATION VARIABLES

3.1 Introduction

The M-Flex 3D printer offers numerous parameters that can be altered within the context of the printing process. All these variables can affect considerably the final structure of the printed object. Therefore, determination of the variables of the printing configuration on the ultimate printed part is imperative for the understanding of the creation of the specimens. However, many of these variables, such as the recoater speed, oscillator speed, X and Y drop spacing, among others, have default settings within the printer and although they can be changed, these modifications were not be addressed in the present research. Many other print setting values given for other parameters are easily defined by the user prior to start the job. For this research, the main variables that will be studied to analyze the influence of printing configuration on the hydraulic properties of the 3D printed specimens are binder saturation, layer orientation and layer thickness.

3.2 Binder Saturation

This parameter is expressed as a percentage and is defined as the fraction of void space between the powder's particles that is filled by furan binder. With , binder saturation can be calculated with the purpose of quantifying how much binder is dispensed into each unit volume. This parameter depends on the drop volume, powder packing rate, drop spacing (X_{sp}, Y_{sp}) and layer thickness (Z_{sp}).

$$Saturation\ [\%] = \frac{100{,}000 * Drop\ Volume}{\left(1 - \frac{PowderPackingRate}{100}\right) * Xsp * Ysp * Zsp} \qquad 3.1$$

The drop volume is measured and calibrated weekly with the drop volume test, which calibrates the print head by measuring the mass of binder jetted in a known number of jet pulses and calculating the average volume of each pulse. The powder-packing rate is the apparent density of the powder being printed, in this case silica sand. The drop spacing is the space between binder drops in the x and y direction, which is static based on the printhead configuration.

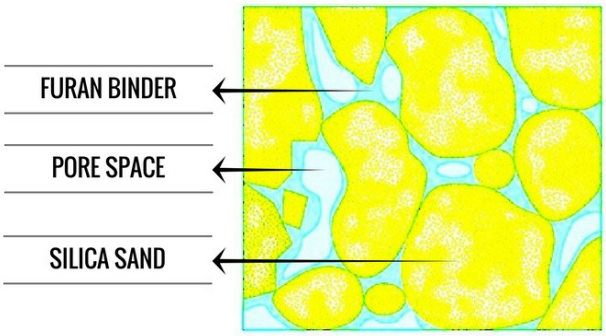

Figure 3.1 Binder Saturation

The schematic shown in Figure 3.1 illustrates the distribution of the binder along the pore space between grains. The yellow zone represents the silica sand grains, while the blue region denotes the furan binder. It is possible to observe that the binder fills the pore space, which implicates that as the binder saturation increases, the final pore space become smaller. This is to say, if the binder saturation is 10%, the binder will occupy one tenth of the initial pore space.

3.3 Layer Orientation

Layer orientation corresponds to the inclination angle of the building layers with respect to the vertical axis. As the object is built up during the printing process, each layer of sand and furan binder is placed over the job box homogenously. However, when varying the position of the same object in space, it is possible that even though the properties in-plane are uniform, the internal arrangement of the solids might be different, which would affect the hydraulic properties of the specimens.

Figure 3.2 illustrates the build-up direction of the cylinders and their rotation along its axis. The angle of rotation is measured with respect to y axes (small black arrows) and the direction of the layer when the cylinder is placed in a vertical position. For instance, from top to bottom in Figure 3.2 the arrangement of the cylinders are 90º, 0º and 45,º being the printing position vertical, horizontal and half inclined respectively.

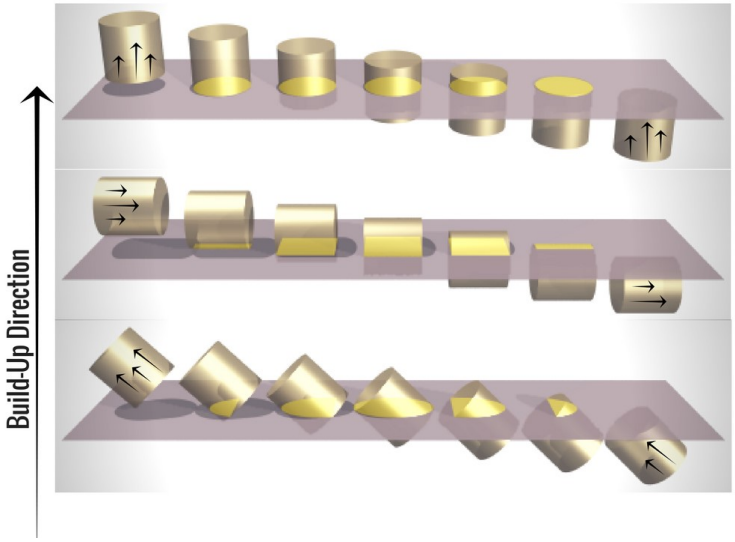

Figure 3.2 Layer Orientation Schematic

3.4 Layer Thickness

Measured in microns, layer thickness is fundamentally the depth of one printing step, between sand recoating and binder dropping from jets, and is directly related to the total number of layers required to fabricate the entire sample. Layer thickness is related to the amount of sand placed along the z axis and corresponds to the Z_{sp} parameter previously stated in as the Z drop spacing. The value given to the layer thickness is easily defined by the user prior to start of a printing job. Figure 3.3 schematically illustrates the thickness of each layer compared with the total height of the cylinder.

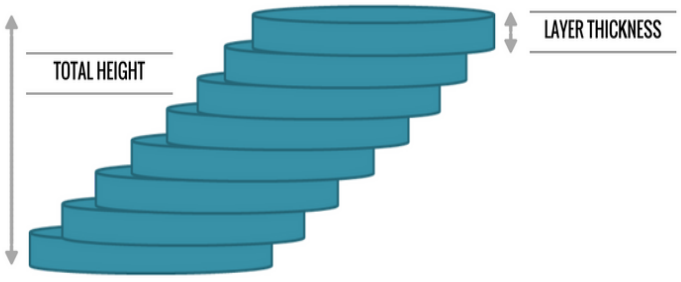

3

Figure 3.3 Layer Thickness Schematic

3.5 Specimens Nomenclature and Testing Matrix

The variation of the parameters described previously, when creating each group of samples generate different pore structures, hence for identification purposes each configuration was assigned with a specific name, as shown in Figure 3.4. The label given for each sample is formed by three main sections; each one of them corresponding to a specific variation in the printing configuration. For binder saturation, four cases were explored: 10%, 15%, 20% and 30%. Layer orientation was addressed by varying the inclination angle from 0° (horizontal specimens), to 45° and 90° (vertical specimens). Finally, the layer thickness of the analogues chosen for this study were 250 µm, 400 µm and 600 µm.

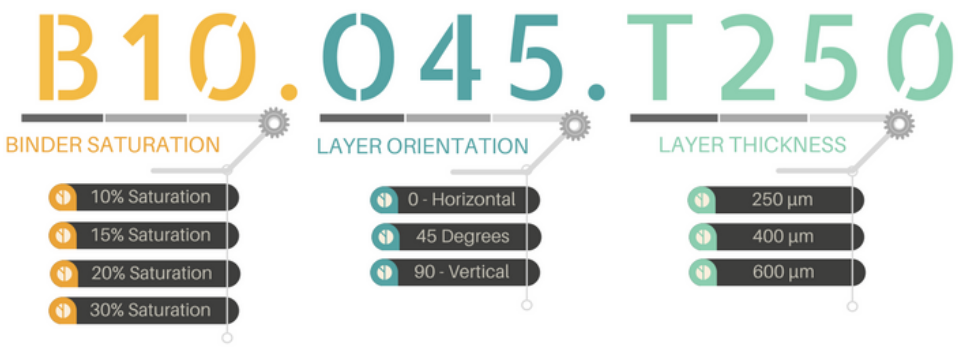

Figure 3.4 Nomenclature of the 3D printing configurations used to identify each set of samples.

For all the testing campaign performed during this study, different printing configurations were used with the purpose of analyzing the influence of these properties on the pore structure and the hydraulic and petrophysical properties. A matrix summarizing the entire test program performed during the present investigation and the variation of the printing configurations per test is presented in Table 3.1

Table 3.1 Matrix of the printing parameters with the type of test performed

Type of Test	Printing Parameters	Calculated Properties
Permeability Test	Binder Saturation: 10% - 20% -30% Layer Thickness: 250 mm Layer Orientation: 0^o - 90^o - 45^o	Initial Permeability Permeability changes with stress
Mercury Injection Test	Binder Saturation: 10% - 15% -20% Layer Thickness: 250 mm - 400 mm - 600 mm Layer Orientation: 0^o - 90^o	Capillary Pressure Curves Pore Size Distribution Porosity
Imbibition Test	Binder Saturation: 10% - 20% - 30% Layer Thickness: 250 mm Layer Orientation: 0^o	Co-Current Imbibition on Fresh Samples
	Binder Saturation: 20% Layer Thickness: 250 mm Layer Orientation: 0^o	Counter-Current Imbibition on Saturated Samples

4 CHAPTER 4 PERMEABILITY TESTING

Prior to starting permeability tests on the 3D printed specimens, it was necessary to ensure whether the furan-silica matrix was going to remain unaffected by the pore fluid intended to be used for the permeability tests. This is important to confirm that any measured permeability values were a result of the 3D printing process and not permeant induced effects. Consequently, the following sections describe an unconfined compression test program to assess the sensitivity of the 3D printed specimens to tap water and silicone. This is followed by the results of the permeability testing program itself.

4.1 Unconfined Compression Strength Tests

Several unconfined compression strength (UCS) tests were conducted varying the type of fluid between tap water and silicone oil, which is known to be an inert liquid, and the time that the specimen remained submerged inside the fluid.

The general procedure for all the specimens after the printing job was finalized was to place the cylinders (1.5 in diameter by 3 in length) into the oven at an optimum temperature of 80°C, for the curing process. After one day of heating treatment, the samples were allowed to cool down for 6 hours. Previous work (Primlukov et al, 2017) found that the time established for the sample to cool down is a key part of the curing protocol. To confirm this impact for this research, three specimens were tested without letting them cool and another 3 specimens after 6 hours of taking them out of the oven. It was found that the strength of the sample was reduced by 20% on average when the sample is not allowed to cool down. Twenty one (21) samples were placed in tap water and another 21 specimens were placed in silicone oil. Three unsaturated specimens were tested immediately following the curing process in order to establish a base case and compare their properties with those obtained from the saturated samples. Once the specimens were placed in either tap water or silicone oil, seven batches of 3 specimens each began to be tested at the following exposure times: 15 minutes, 3 hours, 9.5 hours, 24 hours, 3 days, 1 week and 2 weeks. UCS tests were performed at a constant strain rate of 0.25 mm/min, achieving an average failure time approximately at 2 minutes.

4.1.1 Influence of Water on UCS Peak Strength of the Sandstone Analogues

As shown in Figure 4.1, the strength of water-saturated specimens begins to decrease from an average strength of 23.6 MPa for dry conditions to 17.2 MPa in the first 15 minutes of submersion; which is equal to a reduction of 27.1%.

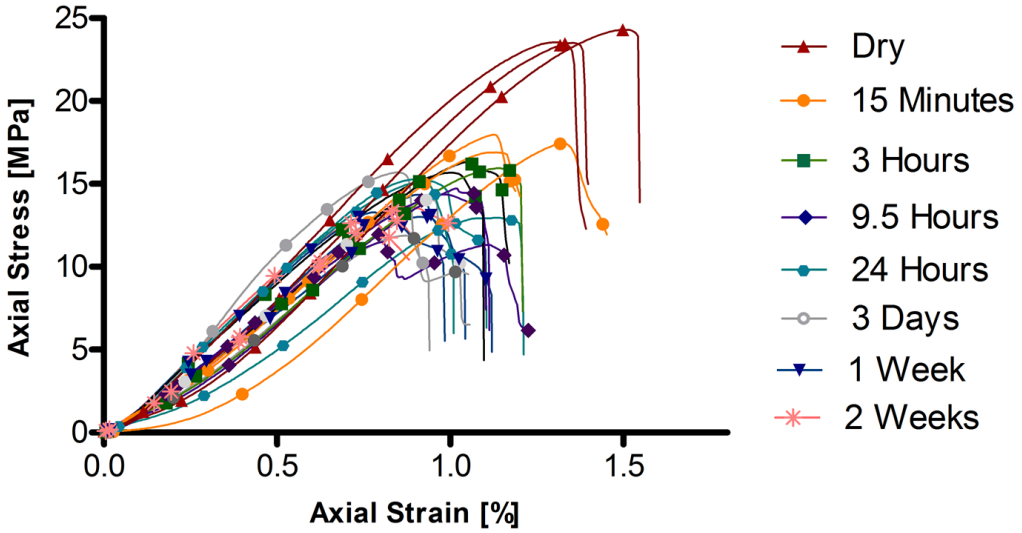

Figure 4.1 Influence of Water on UCS peak strength of 3D printed sandstone analogues – 80°C curing temperature.

Even though the strength of the sample is being constantly reduced with time, eventually, nearly one week after the process started it reaches plateau, where the strength of the sample is reduced by around 42% on average compared with the strength of the dry samples.

On the other hand, with the purpose of determining the impact of the curing temperature in the UCS peak strength of the samples, the same procedure described for specimens cured at 80°C, was performed with a curing temperature of 110°C. As shown in Figure 4.2, the strength of the water soaked samples, for a curing temperature of 110°C, was reduced by 50% on average compared with the strength of the dry samples. It was also observed that there is a substantial reduction in the sample's UCS peak strength in comparison with those values obtained for a curing temperature of 80°C, which it is attributed to the fact that temperatures over 80°C during the curing process,

lead to a loss of strength, primarily as a result of reaction kinetics of the furan binder. Similar results were obtained by Primkulov et al., (2017). Moreover, before the samples reach the final UCS peak, several reductions on the strength (i.e. as it were false peaks) were appreciated on some curves, this behaviour might be related to heat-induced disturbance generated within the matrix of the sample, which results in some apparent weakening of the specimen.

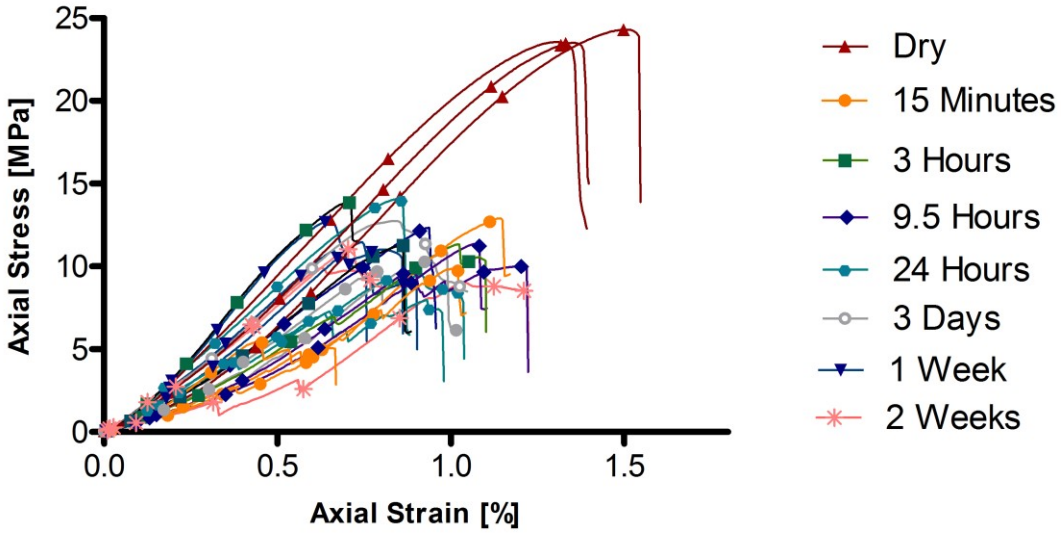

Figure 4.2 Influence of Water on UCS peak strength of 3D printed sandstone analogues – 110°C curing temperature.

4.1.2 Influence of Oil on the UCS Peak Strength of the Sandstone Analogues.

For silicone oil soaked specimens, behavior of the stress strain curves for all the submersion times was analogous to those for the dry samples, which implies that the submersion of the specimens in silicone oil is not affecting the strength of the cured furan binder. An average UCS peak strength of 22.8 MPa was found from this series of tests, which compares favorably with the UCS of 23.6 MPa achieved for the dry samples in the water saturated test series. It is also possible to discern, from the results shown in Figure 4.3, that the strength of the sample was reduced by 5% on average compared with the strength of the dry samples. However, taking into account the percentage error of the loading frame, the reduction of the strength for the samples could be lower than 5%.

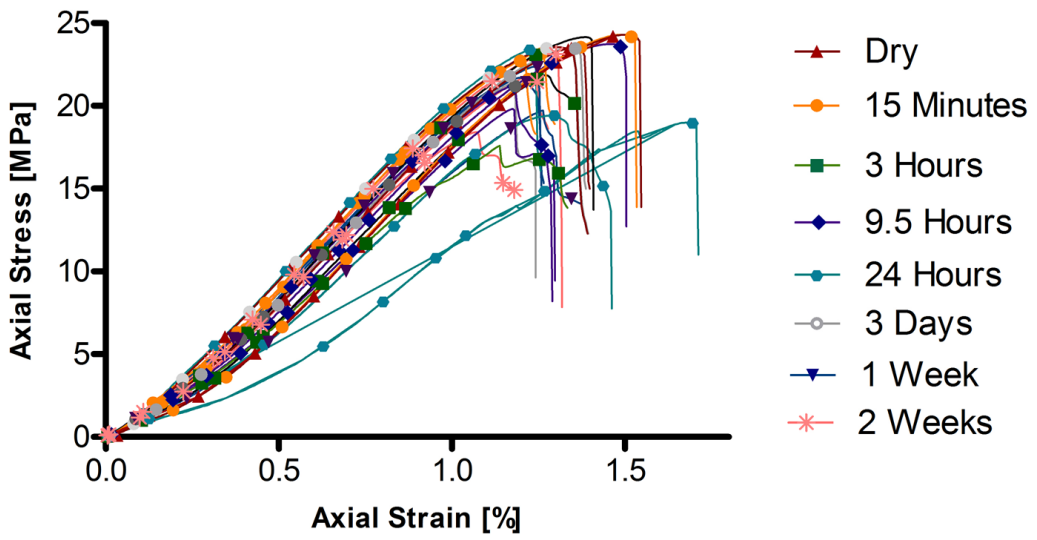

Figure 4.3 Influence of Silicone Oil on UCS peak strength of 3D printed sandstone analogues - 80°C curing temperature.

4.1.3 Influence of cyclic wetting and drying on UCS Peak Strength of analogues.

A distinct experiment was performed with the purpose of determine how much strength can be recovered if the specimens soaked in water were placed into the oven again. The samples were placed in water for the same time lapses as the previous practices, subsequent they were placed into the oven at 80°C for a period time of 24 hours. Once the water was evaporated, the UCS test was performed. Figure 4.4 shows the results obtained.

The results obtained for this section indicate that the mechanical properties of the 3D printed specimens have a different degree of deterioration after wetting and drying when compared with those properties of the wet samples. Figure 4.4 shows that the specimen's behavior after wetting and drying cycles is becoming more ductile as opposed to the brittle behavior of the dry specimens. Hua et al. (2015) investigated the influence of cyclic wetting and drying on sandstone and found that after seven wetting and drying cycles the sandstone samples became more softened and ductile, showing that these cycles have an obvious influence on the failure characteristics of the specimens. However, although the samples are becoming more ductile, the UCS peak strength of

the 3D printed specimens was reduced by 20%, meaning that the average peak strength of the cylinders after being subjected to a cycle of wetting and drying is 18.8 MPa.

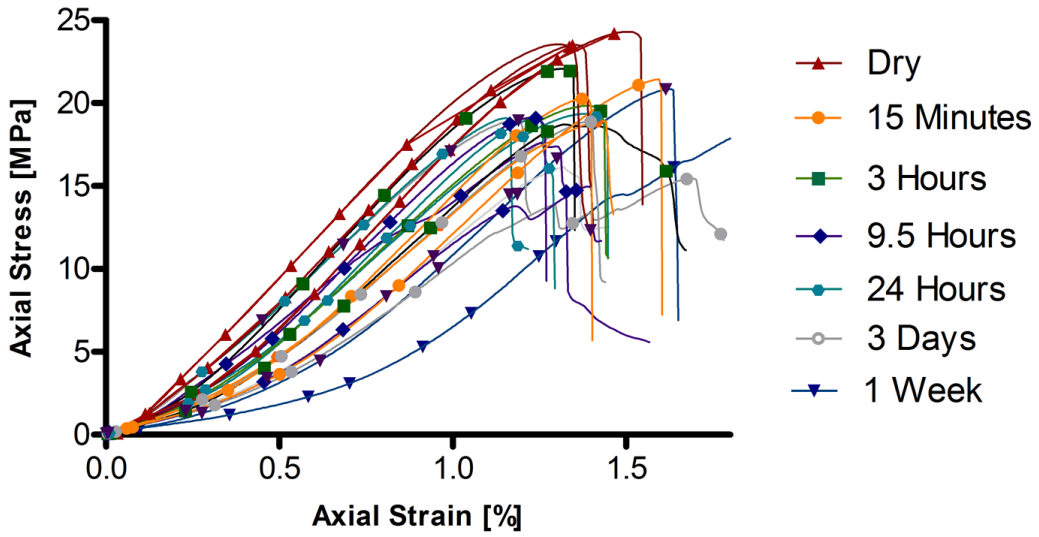

Figure 4.4 Stress Strain curve for different periods of time when the specimen is subjected to a wetting and drying cycle.

4.1.4 Summary of the UCS testing campaign

By analyzing the trend of the UCS peak strength of specimens saturated with both fluids and their exposure time, it was possible to confirm whether the sandstone analogues were or were not going to have any strength or structural effects that might generate an anisotropic volumetric behavior when subjected to the planned effective confining stress levels during permeability tests. Results showed that for the cylinders submerged in water, the UCS peak strength was reduced by an average of 42% with respect to the unsaturated case (i.e. base case), whereas for the specimens submerged in silicone oil, UCS peak strength was reduced by an average of 5%. It was therefore concluded that silicone oil would be used as the permeant for all permeability testing.

4.2 Test Facility and Permeability Experimental Considerations

After gathering and combining the information regarding the incidence of pore fluids and curing temperatures on the specimens' matrix, silicone oil (174.25 cP of viscosity, determined using a Cambridge viscometer 2000) was selected as the fluid to perform the permeability tests, performed on 24 hour-cured specimens.

As a standard procedure to fully saturate the specimens, all cylinders were placed into a closed vessel full of silicone oil right after their curing time was ended. Additionally, before placing the sample inside the cell, each specimen was vacuumed for a time period of four hours (Selvadurai and Głowacki 2008). Finally, once the experimental setup was completed, specimens were allowed to saturate overnight under an effective confining stress of 500 kPa as a result of a confining stress of 2.5 MPa and back-pressure (i.e. pore pressure) of 2.0 MPa.

A NMC-6500 triaxial cell was used to perform the permeability tests. 3D printed cylindrical specimens with dimensions of 38.1 mm diameter and 76.2 mm height were mounted on a pedestal, which had the same diameter as the specimens, set at the base of the triaxial cell. The cell base contains two entry ports to provide fluid flow into the sample. Between the specimen and the base, a filter paper and a pore stone were placed in order to assure a homogeneous entrance of oil flow. Similar configuration was used at the top of the sample; a top cap was placed on the sample to connect the top-back pressure line. Once the sample was placed on the base, two latex membranes were stretched over the sample, the base pedestal and top cap. Two pairs of 38.1 mm diameter (1.5 in.) viton o-rings, 2 at the bottom and 2 at the top section, were installed to seal the membrane against the platens. This set up is intended to be used as a secure isolation system for the sample from the external medium and to create the adequate conditions to run permeability experiments. A representative layout of the experimental setup described previously is shown in Figure 4.5.

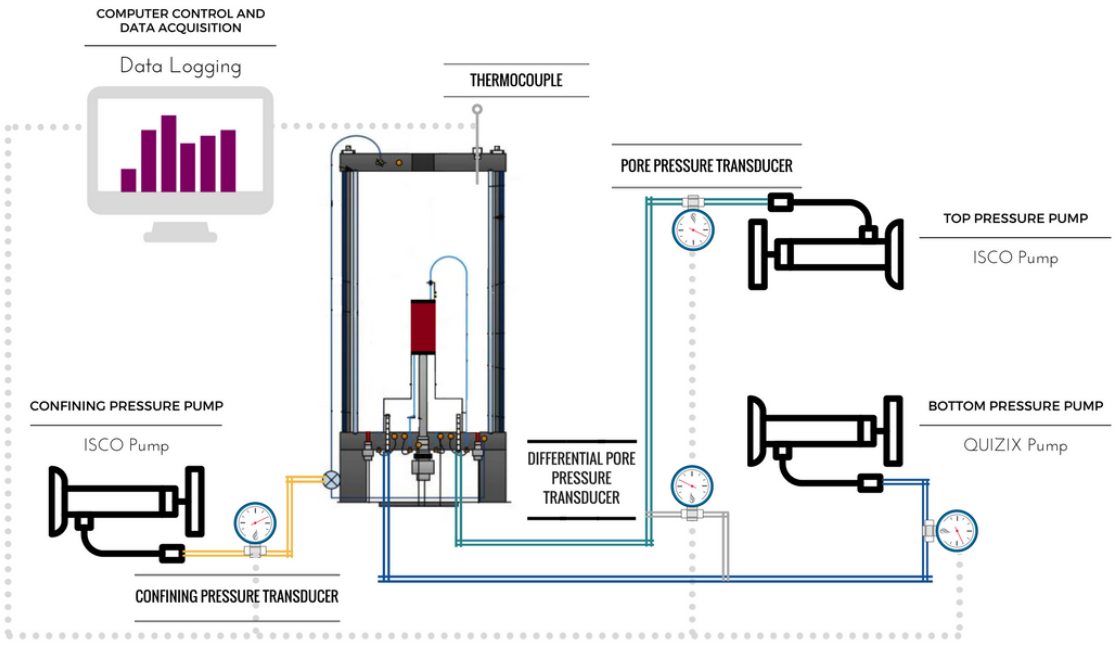

Figure 4.5 Complete setup used for the permeability tests.

Specimens were subjected to a cycle of loading and unloading consisting in 9 different effective confining stresses, 500 kPa, 1000 kPa, 2500 kPa, 5000 kPa and 10000 kPa. At each stage a permeability test was performed with the purpose of analyzing permeability variations when the samples are subjected to different confining pressures. All permeability tests were performed at room temperature and at a fixed flow rate (pumping from the bottom of the sample using the QUIZIX pump to the top of the cylinder with the ISCO pump) measuring the differential pressure across the sample at steady state. The apparatus used for this measurement was a differential pressure transducer (Validyne DP15TL) with maximum capacity of 550 kPa and accuracy of ± 2.75 kPa. At low effective confining stresses (<5000 kPa), steady state was easily reached at a flow of 1 mL/min. Nevertheless, at high effective confining pressures achieving constant differential pressures across the sample exhibited longer stabilization times, hence the flow rate was reduced to 0.5 mL/min and a volume equivalent of 4 pore volumes was displaced along the sample.

4.3 Permeability Experimental Results and Analysis

4.3.1 Influence of Layer Thickness in Permeability

The relationship between hydrostatic compression and the variation of layer thickness with the 3D printed specimens' permeability is plotted in Figure 4.6. Three different scenarios were studied in the variation of layer thickness; horizontal, vertical and 45°. For all the cases, when varying the layer orientation, independently of their inclination, the range of values for each consolidation step below a 5000 kPa effective confining stress is showing almost no variation.

Detailed information about each specimen, such as the variations along the test on the flow rate and differential pressure, is presented in Table 4.1. Additionally, the value of permeability for each sample can be found in this table to facilitate the understanding of this parameter's behavior. The flow rates achieved along the test, as it is stated in Table 4.1, are below 2 ml/min. Low flow rates were maintained with the purpose of achieving steady state (constant differential pressure along the core for a specific period of time), but at the same time assuring a differential pressure above 50kPa since pressures below this value are out of range for the diaphragm (in the differential pressure transducer) that is being used for these tests.

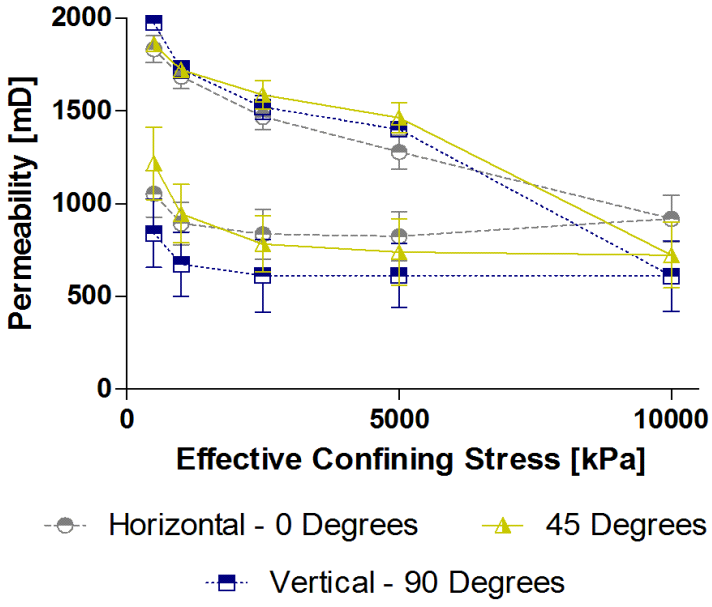

Figure 4.6 Permeability vs Effective Confining Stress for Different Layer Orientation.

Table 4.1 Summary of Parameters for Permeability Test Performed Varying the Layer Orientation of the 3D Printed Specimens.

Confining Pressure [kPa]	Effective Stress [kPa]	Flow Rate [ml/min]			ΔP [kPa]			Permeability [mD]		
		B10.O90.T250								
		S1	***S2***	***S3***	***S1***	***S2***	***S3***	***S1***	***S2***	***S3***
2500	500	1	2	1	98	195	103	2004.03	2014.30	1906.74
3000	1000	2	2	1	219	225	120	1793.56	1745.73	1636.62
4500	2500	2	1	1	240	139	130	1636.62	1412.91	1510.73
7000	5000	2	1	1	277	142	140	1418.01	1383.06	1402.82
12000	10000	0.5	2	0.5	121	570	430	811.55	790.32	228.37
7000	5000	2	2	0.3	477	561	220	823.458	745.00	270.27
4500	2500	2	2	0.5	486	485	450	808.20	809.88	218.22
3000	1000	2	2	0.5	467	460	300	841.09	853.89	327.32
2500	500	2	2	0.5	386	380	208	1017.58	1033.66	472.10
B10.O0.T250										
		S1	***S2***	***S3***	***S1***	***S2***	***S3***	***S1***	***S2***	***S3***
2500	500	2	1	1	208.5	102	116	1883.88	1925.43	1693.05
3000	1000	2	1	1	221	114	126	1777.32	1722.76	1558.68
4500	2500	1	1	1	133	124	146	1476.65	1583.82	1345.16
7000	5000	0.5	1	0.5	80	135	85	1227.46	1454.77	1155.26
12000	10000	0.5	0.4	0.4	125	67	98	785.578	1172.50	801.61

7000	5000	0.5	1	0.4	138	186	119	727.387	1085.05	660.15
4500	2500	0.5	1	0.5	140	178	140	701.409	1103.34	701.40
3000	1000	0.5	1	0.4	118.3	176	102	830.0705	1115.879	734.1858
2500	500	0.5	1	0.4	119	156	73	825.1878	1258.94	1076.135

B10.O45.T250

		S1	***S2***	***S3***	***S1***	***S2***	***S3***	***S1***	***S2***	***S3***
2500	500	1	1	-	105	106	-	1870.43	1852.78	-
3000	1000	1	1	-	112	116	-	1753.52	1693.06	-
4500	2500	1	1	-	118	130	-	1664.36	1510.73	-
7000	5000	1	1	-	127	142	-	1546.41	1383.06	-
12000	10000	0.5	0.5	-	109	180	-	900.89	545.54	-
7000	5000	0.5	0.4	-	107	140	-	917.73	561.13	-
4500	2500	0.5	0.8	-	105	249	-	935.21	630.99	-
3000	1000	1	1	-	178	249	-	1103.34	788.73	-
2500	500	1	1	-	139	192	-	1412.91	1022.89	-

There are some important aspects that should be pointed out: first, assuming a negligible influence of the initial effective confining stress (500 kPa) on the volume change within each specimen, the initial permeability value for the 3D printed specimens is repeatable and consistent among each specific configuration. Second, the value of the initial permeability of the 3D printed sandstone specimens is essentially identical, between 1.8 D and 2 D, regardless of the inclination of the building layers used for their fabrication (Figure 4.6).

The implication that the orientation of the building planes has no clear influence on the hydraulic properties of the analogues is contrary to the results obtained by several authors (De Silva et al. 2014, De Silva et al. 2016, Corbett et al. 1992, Ringrose et al. 1994, and Lake et al. 1991) where heterogeneous rock permeability values generated by the presence and orientation of either bedding planes or lamination with respect to the experimental flow direction, on natural sandstones, implied a variation on the measured fluid velocity (Darcy flow) and hence on the permeability measurements. It would appear that 3D printed sandstone's permeability seem to remain unaffected by the layer orientation used on their manufacturing process, as shown in Figure 4.7, where building direction of the specimens is denoted. The small arrows represent the direction of flow when performing the permeability tests.

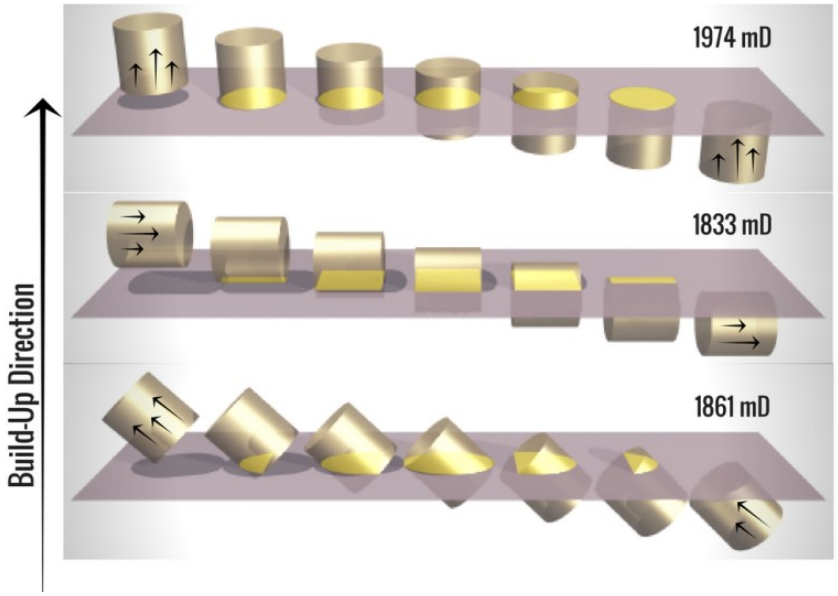

Figure 4.7 Variation of 3D Printed Analogues Permeability with Respect to Building Layer Orientation

These results might indicate that the building process' influence has zero to minimal impact on the homogeneity of the transport properties throughout the specimen's body. This hypothesis was initially considered and addressed because of the strong influence of the building planes' orientation on the failure mode exhibited by the same type of 3D printed specimens tested by Gomez Ramirez et al. 2017. This failure behavior is thought to be triggered by the direct effect of the applied load on the layers, which are attributed to be planes of weakness along which cracking can develop. Consequently, binder concentration and distribution on this "layer-layer interphase", may differ to the one encountered within the actual sand layer, generating anisotropic measurements on the transport properties.

Independent of the printing configuration used on the manufacturing process, the 3D printed sandstone specimens pore space is experiencing an appreciable irreversible deformation as the effective confining stress is increased above 5 MPa. This effect is clearly evidenced in Figure 4.6, where a notable reduction of the specimens' permeability is represented by a steeper declining trend of the slope after reaching this stress value. In addition, a significant hysteresis of permeability occurs during the unloading portion of the test. The magnitude of the permeability decrease during loading remains unrecovered after unloading to approximately 5 MPa and a minor recovery in the permeability value occurred once the effective confining stress was reduced to 1.0 MPa

With the purpose of analyzing the response of the matrix and pore space to compressive stress, after each test was completed, a representative section of the cores B10.O0.T250 were studied using two different imaging tools: 1) optical microscopy and 2) scanning electron microscopy (SEM). Pore space configurations from each stress level was compared with an undisturbed 3D printed specimen, built with the same properties, looking for any structural changes generated because of the compressive stress.

4.3.2 Imaging Tools

Results obtained from SEM are shown in Figure 4.8, where there is a physical evidence of a structural variation in the pore space of the samples for various effective confining stresses. In fact,

there is a change in the grain structure evidenced by the rearrangement of the grains, which tend to form clusters of particles in specific zones as a result of the anisotropic distribution the compacting stress throughout the body of the specimen. This deformed arrangement contrasts with the in-plane uniformity exhibited by the undisturbed sample, which contrary to any natural material that might be object of study of this same type of research, has no previous stress history and is being tested after being printed.

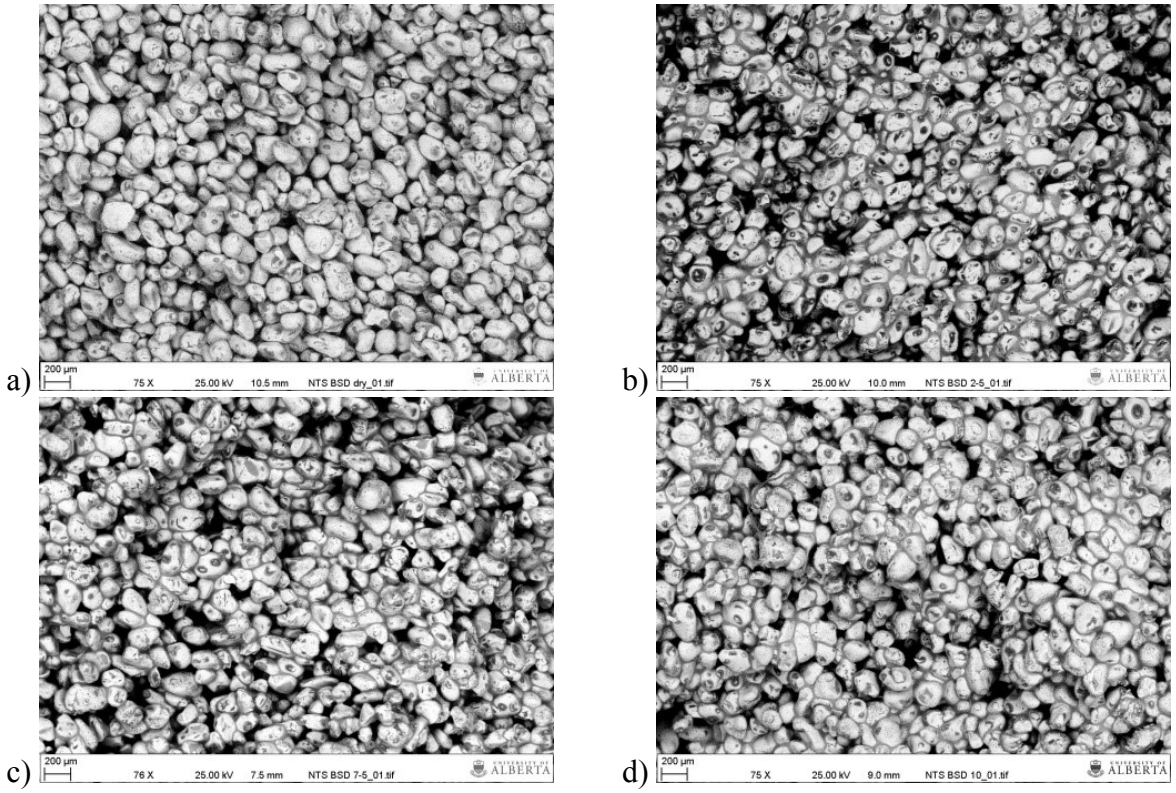

Figure 4.8 SEM images for different levels of hydrostatic effective confining stress applied on 3D printed sandstone analogues (a) original specimen (b) 2.5 MPa of confinement (c) 7.5 MPa of confinement (d) 10 MPa of confinement.

Further measurements of the areal distribution of both silica particles and void space within the planes for each SEM image were performed by converting each picture into binary images and calculating the amount of pixels' corresponding to either "white zones" (grains) or "black zones" (pores). Results show that for the undisturbed sample illustrated in Figure 4.8 (a), 66.3% of the

surface of the picture is constituted by grains, while for 2.5 MPa (b), 7.5 MPa (c) and 10 MPa (d) effective confining stress, the average grain surface is 58.0%. It should be noted that for high porosity sandstones, grains are loosely packed and the pore-throat size is comparable to the actual pore size. In such conditions, the cataclastic deformation is probably generated mainly by grain sliding and rotation (Ehrlich et al. 1991 and Bernabé et al. 2003). Therefore, such structure deformation might result in a pore throat collapse phenomenon, which can cause an increase of non-effective porosity throughout the microstructure of the specimen and hence a decrease in its permeability.

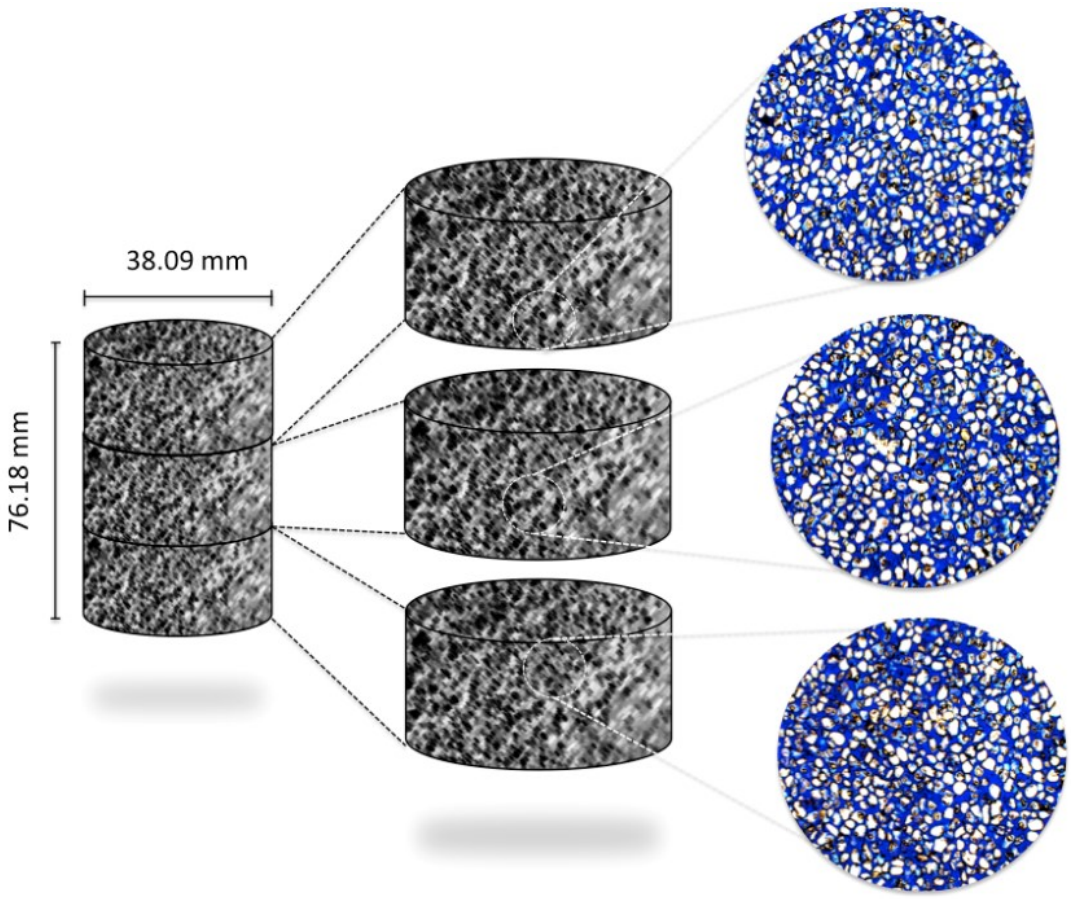

Figure 4.9 3D Printed pore structure uniformity before subjected to hydrostatic loading tests

Complimentary studies were conducted on the sandstone analogue sections using optical microscopy imaging (OM). OM images of the 3D printed specimens were divided into three sections; top, middle and bottom as shown in Figure 4.9. Analyses performed on each picture using

the same binary-conversion method formerly used on the SEM images resulted in an average grain area of 34.4 ± 0.12% when combining the three sections.

The appreciable grain agglomeration and pore structure deformation phenomena, observed on the SEM images, is also evident when comparing the OM images resulting from the compacted samples with the undisturbed specimen. By performing a grain-to-grain contact analysis on the plane exposed by the picture, and identifying the number of remaining connections from grinded grains, which were previously attached to overlying plane of the specimen, it was feasible to qualitatively characterize the grain packing and present evidence of the microstructure deformation of the sandstone analogues.

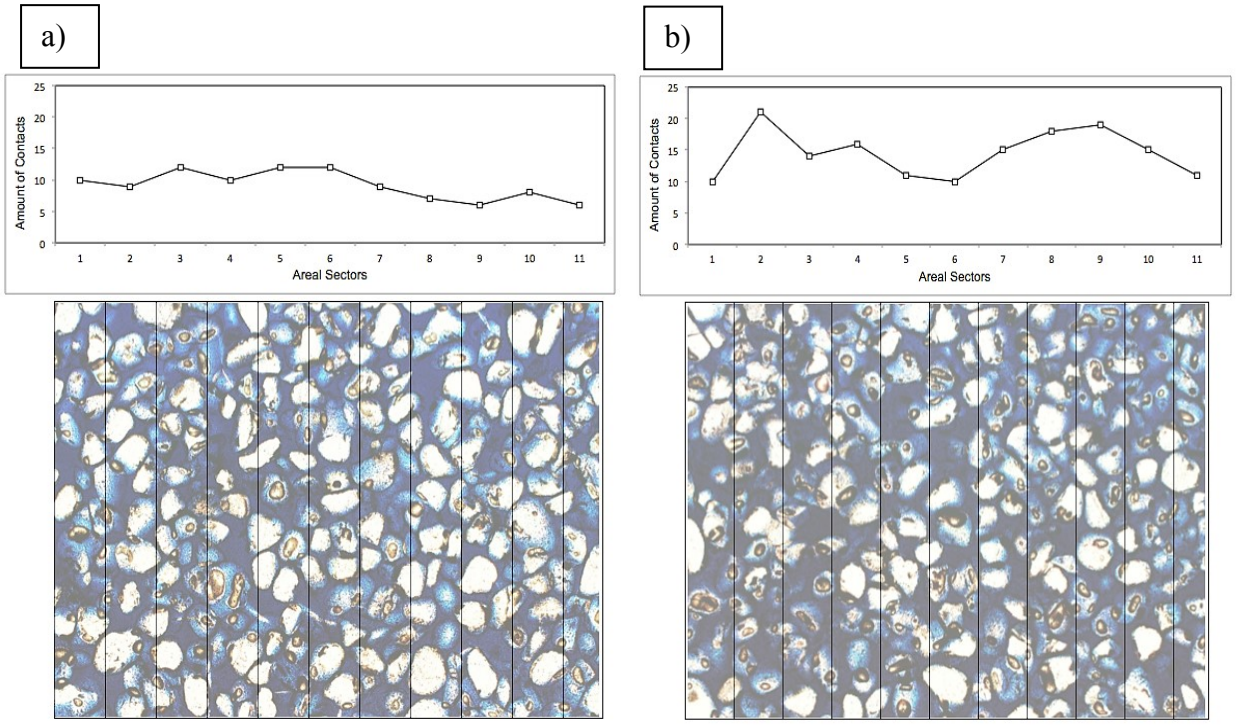

Figure 4.10 Comparison between the amount of contacts present on the undisturbed and 10 MPa-confined sandstone analogue.

Using the same image processing software, it was possible to divide the OM images into eleven equivalent-area sections, as shown in Figure 4.10. Afterwards, by converting the image into a colored 8-bit picture and thresholding their color distribution, it was possible to enhance the contrast between the contacts (darker bean-shaped spots) and the rest of the structure. The microstructure of the base case section, Figure 4.10a, exhibits a higher surface covered by grains

and uniformly distributed grain contacts throughout the entire area of the image. On the other hand, Figure 4.10b corresponds to the 3D printed analogue subjected to 10 MPa effective confining pressure and shows an appreciable increase in the number of contacts displayed by each section in comparison with the undisturbed specimen.

These findings suggest a clear indication of the structure deformation and grain re-organization experienced by the specimens as a response to increased effective confining stresses, as expected.

4.3.3 Influence on Binder Saturation in Permeability

The variation of permeability when increasing the amount of binder placed into the sample (i.e. binder saturation) is remarkable. As shown in Figure 4.11, specimens built up with 20% furan saturation showed an average permeability of 1,046 mD, which implies a 42.8% reduction in their initial permeability when compared to the 10% saturation specimens, which had an average permeability of 1,833 mD. As suggested previously by Panda and Lake (1995), increments of the amount of cementing material existing within the porous media of an unconsolidated sandstone, increases the effective contact area of the particles and elevates the effective tortuosity of the media, generating a decrease in the value of the rock's permeability.

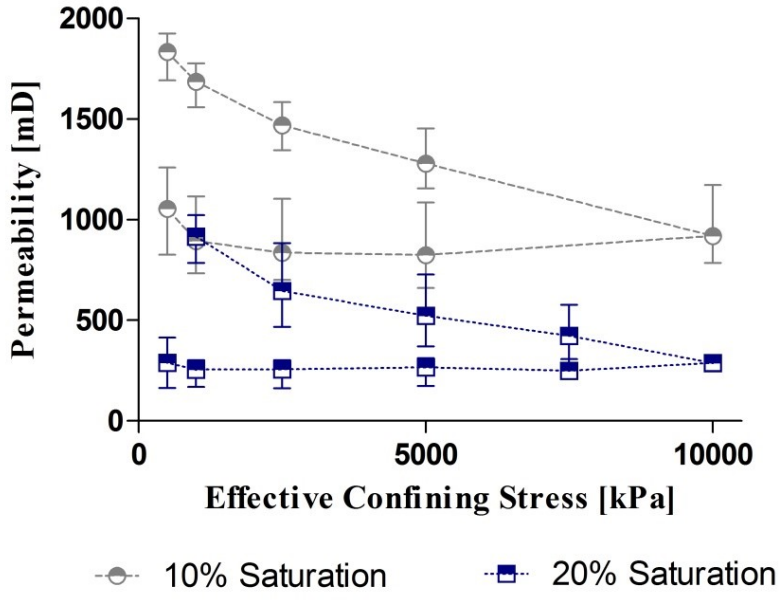

Figure 4.11 Permeability vs Effective Confining Stress for different Binder Saturations

However, once the specimens are subjected to a higher level of effective confining stress reached throughout the test (10 MPa), the 20%-saturation samples reach a maximum average permeability reduction of 27%, comparing the initial (freshly-printed) and final (after compaction) values; whereas for 10%-saturation specimens, the average percentage reduction observed was 55%. This behavior suggests that the cylinders manufactured using 10% furan saturation is more sensitive to stress changes than those of 20% saturation. Once more, the results obtained by Gomez-Ramirez et al. 2017 support this tendency since it was found that there is a direct relationship between furan saturation and UCS peak strength of 3D printed samples. An increase of 39.9% on the analogue's peak UCS strength is achieved when increasing the furan saturation from 10% to 20%.

Natural rocks such as Berea sandstone, have a permeability that ranges between 0.114 D to 1.168 D with porosities that vary between 19% and 26% (Churcher et al. 1991). Fontainebleau sandstone have a permeability that ranges between 0.592 D to 0.912 D with porosities that oscillates between 15% and 19% (Gomez et al. 2010). Simplifying the data presented previously, a direct comparison between natural and manufactured materials implies an average increase of 41.6% with respect to the upper case of Berea sandstone's permeability value and of 54.4% with respect to the upper case of Fontainebleau sandstone for 10% binder saturation specimens. In samples printed with 20% saturation the values of the permeability are more in accordance with those natural rocks with high values of permeability. However, the reduction of the permeability is exclusively due to the increase in the amount of cementing material (binder) and not because of a better rearrangement of the grains. Further studies must be done to reduce the permeability of the specimens by varying the structure of the sample during the printing process and not decreasing the percentage of pore space by filling it with more binder material.

Permeability changes when subjected to different confining stresses were also measured for cylinders printed with 30% binder saturation. For this case, two specimens were printed and cured at 80ºC. As shown in Figure 4.12, the results obtained suggest that specimens printed with 30% binder saturation highly differ one to the other one. The high range in the error bars shown in the permeability vs effective confining stress curve suggests that the repeatability of the specimens when printing with this amount of binder saturation cannot be assured. Previous studies (Wang et al. 2003, Cueto-Felgueroso and Juanes, 2009 and Chapwanya and Stockie, 2010) indicated that the infiltration phenomenon of any fluid into a non-saturated pore structure is driven by the

relationship between gravitational forces (which tend to destabilize the system) and viscous forces (which tend to stabilize the system). As the temperature of the build box within the M-Flex system is cooler than that used for curing the specimens (despite the usage of the recoater heating system), a portion of the recently sprayed binder will not be polymerized and will remain as a fluid inside the body of the just printed specimen. When the weight of furan is high enough to overcome the viscous forces that lock it up inside the bounded zones, it will tend to drop out of its theoretical placement and move towards saturated regions. This phenomenon will generate both dimensional inconsistencies and a gradient of furan distribution throughout the volume of the specimen that is being built. In general, the majority of the non-cured binder will be located at the bottom of the sample, behavior that is highly influenced by the enhanced relative permeability to furan that the already saturated zones possess. When energy is high enough, the binder will even tend to come out of the saturated regions and imbibe into the unsaturated ones.

This phenomenon is thought to be generating inconsistencies on the theoretical behavior that this group of specimens should exhibit (i.e. reduced permeability with respect to 20% saturation specimens). Because of the increased volume of furan that is sprayed by the printing head to build the 30% saturation specimens, a binder-saturation gradient could have been generated along the body of the specimens, which will induce the existence of highly-impregnated zones as well as poorly-saturated ones and therefore heterogeneous induced pressure gradient, which influences the permeability calculations, and low repeatability of the results.

One of the specimen's permeability resulted to be comparable to the 10%-saturation's average permeability, while the second one exhibited a value equivalent to the permeability of a 20%-saturation analogue. These outcomes might suggest that there is a different volume of binder inside the body of the specimens, nonetheless, as this possibility can be discarded due to the precision of the printer at the moment of binder deposition and also because it was no fluid bleeding noticed outside the theoretical shape of the cured cylinders, these variations are solely related to the distribution of the furan binder across the volume of the sandstone analogues. One of the analogues is behaving as if it had the volume of binder of a 10%-saturation specimen and the other one as a 20%-saturation one.

These inferences allow concluding that there is a strong influence of high volumes of binder saturation on the permeability of the sandstone analogues. The induced heterogeneous distribution

of binder inside the body of the specimen might turn out being detrimental when the main intention of the manufacturing process is to emulate stronger and less permeable reservoir formations.

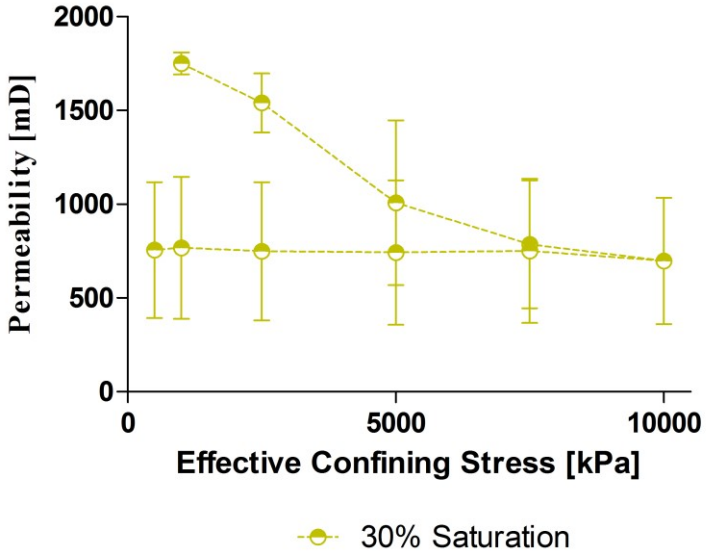

Figure 4.12 Permeability vs Effective Confining Stress for 30% Binder Saturation

Detailed information about each specimen, such as the variations along the test on the flow rate and differential pressure, is presented in Table 4.2. Additionally, the value of permeability for each sample can be found in this table to facilitate the understanding of the variation of the binder saturation on the 3D printed sandstone analogues. The flow rates achieved along the test for specimens printed with 20% saturation, as stated in Table 4.2, are lower than those reached in the test performed for 10% saturation. As the permeability is lower, the flow rates were decreased with the purpose of achieving steady state easily.

Table 4.2 Summary of Parameters for Permeability Test Performed Varying the Binder Saturation of the 3D Printed Specimens.

Confining Pressure [kPa]	Effective Stress [kPa]	Flow Rate [ml/min]			ΔP [kPa]			Permeability [mD]		
		B10.O0.T250								
		S1	***S2***	***S3***	***S1***	***S2***	***S3***	***S1***	***S2***	***S3***
2500	500	2	1	1	208.5	102	116	1883.88	1925.43	1693.05
3000	1000	2	1	1	221	114	126	1777.32	1722.76	1558.68
4500	2500	1	1	1	133	124	146	1476.65	1583.82	1345.16
7000	5000	0.5	1	0.5	80	135	85	1227.46	1454.77	1155.26
12000	10000	0.5	0.4	0.4	125	67	98	785.578	1172.50	801.61
7000	5000	0.5	1	0.4	138	186	119	727.387	1085.05	660.15
4500	2500	0.5	1	0.5	140	178	140	701.409	1103.34	701.40
3000	1000	0.5	1	0.4	118.3	176	102	830.0705	1115.879	734.1858
2500	500	0.5	1	0.4	119	156	73	825.1878	1258.94	1076.135
		B20.O0.T250								
		S1	***S2***	***S3***	***S1***	***S2***	***S3***	***S1***	***S2***	***S3***
2500	500	1		0.5	-					
3000	1000	1	0.5	0.4	208.85	96	100	940.36	1022.89	785.58
4500	2500	0.5	0.2	0.3	111	84	101	884.661	467.61	583.35
7000	5000	0.4	0.2	0.3	108	106	126	727.388	370.56	467.61
9500	7500	0.4	0.2	0.3	136	140	144	577.631	280.56	409.16

12000	10000	0.2	0.2	0.2	135	159	121	290.955	247.04	324.62
9500	7500	0.2	0.2	0.2	180	175	128	218.22	224.45	306.87
7000	5000	0.5	0.2	0.2	317	226	126	309.77	173.80	311.74
4500	2500	0.5	0.2	0.2	325	241	130	302.15	162.98	302.15
3000	1000	0.5	0.2	0.2	325	233	134	302.15	168.58	293.13
2500	500	0.2	0.2	0.3	173	239	142	-	164.35	414.92

B30.O0.T250

		S1	***S2***	***S1***	***S2***	***S1***	***S2***
2500	500	0.5	0.7	54	62	1818.47	2217.36
3000	1000	0.5	0.7	58	76	1693.06	1808.90
4500	2500	0.3	0.7	71	81	1383.06	1697.24
7000	5000	0.2	0.7	69	95	569.26	1447.12
9500	7500	0.2	0.7	88	122	446.35	1126.85
12000	10000	0.2	0.7	109	121	360.36	1033.66
9500	7500	0.2	0.7	107	121	367.09	1136.17
7000	5000	0.2	0.7	110	122	357.08	1126.85
4500	2500	0.2	0.7	103	123	381.35	1117.69
3000	1000	0.2	0.7	101	120	388.90	1145.64
2500	500	0.2	0.7	100	123	392.79	1117.69

4.3.4 Pore Compressibility

The corresponding coefficient of pore compressibility with respect of effective confining stress is plotted in Figure 4.13. This parameter (Zimmerman 1991) was measured by varying the confining stress and recording the variations of volume in the pumps while holding a constant pore pressure of 2 MPa (Equation 4.1).

$$C_{pc} = \frac{-1}{V_p^i}\left(\frac{\partial V_p}{\partial P_c}\right)_{P_p} \tag{4.1}$$

where V_p^i corresponds to the initial pore volume of the specimen, calculated by $V_p^i = \phi V_b$, and ∂V_p is the change in pore volume generated by an increase/decrease in the confining stress (∂P_c).

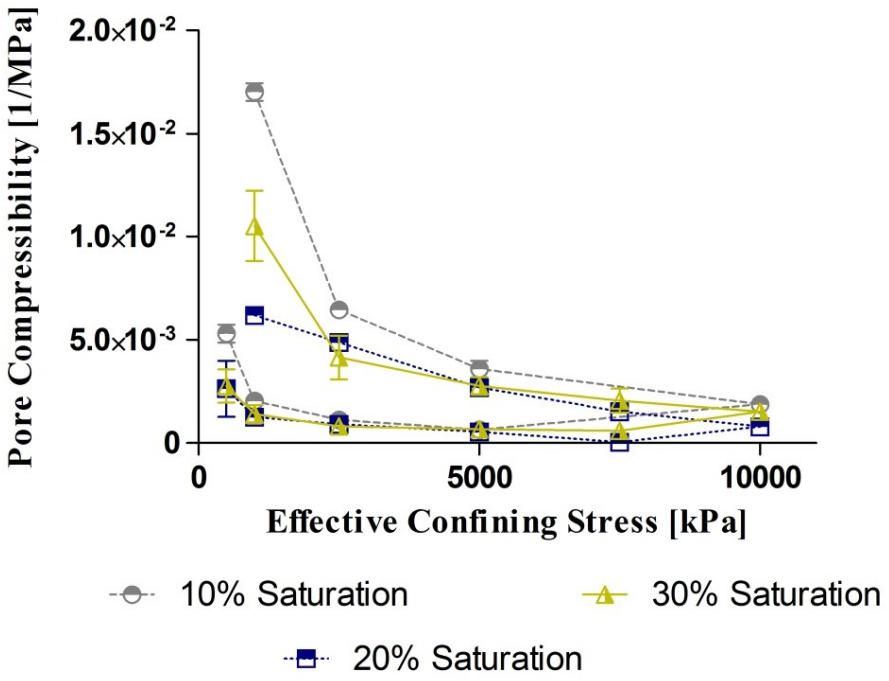

Figure 4.13 Pore Compressibility vs Confining Stress for Different Binder Saturations

Figure 4.13 shows the values of pore compressibility calculated for specimens printed with 10%, 20% and 30% binder saturation. The bullet in the figure represents the mean value, while the error bar denotes the range of maximum and minimum value of pore compressibility obtained. For all cases, a gradual decrease on the pore compressibility of the sample is observed with continuous increments of the effective confining pressure during the loading portion of the curve. During the unloading section, the value of the pore compressibility seems to be constant until reaching the last two stages of unloading, where there is an increment on the value calculated. A similar behavior is obtained in the permeability vs effective confining stress curve where a small portion of the permeability is recovered at the last two stages. This parameter had a good repeatability for 10% and 20 % binder saturation specimens; however, specimens printed with 30% saturation presented a higher variability in the values calculated. The explanation of this behavior was explained earlier in this chapter.

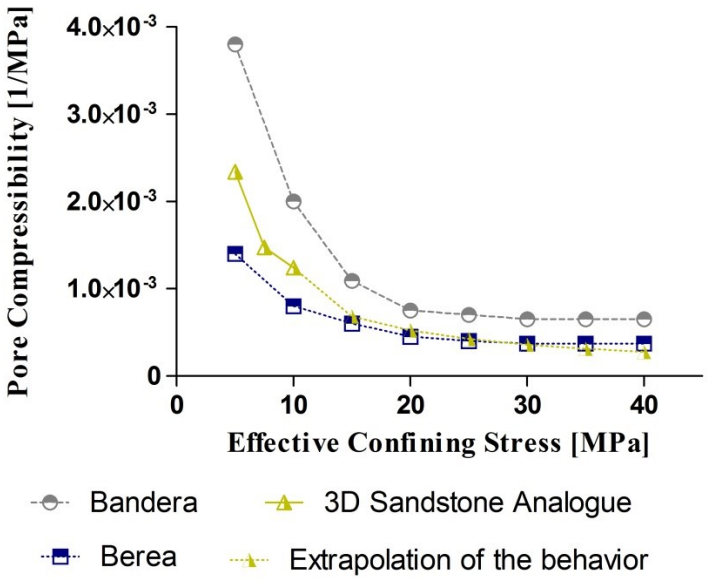

Figure 4.14 Pore Compressibility curves from Natural Sandstones and 3D Printed Sandstone Analogues

Experimental data collected by (Zimmerman 1991) was plotted on Figure 4.14 with the purpose of comparing the pore compressibility of the 3D printed sandstones with data obtained from common and deeply studied natural sandstones. Changes in pore compressibility when the

specimen is subjected to different confining stresses (up to 40MPa), of Berea and Bandera sandstones, are shown in Figure 4.14. Nonetheless, the maximum effective confining stress applied during the experiments conducted in this study was 10 MPa, therefore an exponential approximation of the behavior of the compressibility of the sandstone analogues was used to extrapolate the results up to the range of confining pressures covered by the natural materials' data.

As observed in the results plotted in Figure 4.14, the pore compressibility of the 3D printed sandstone is in considerably good accordance with the results obtained from both Bandera and Berea Sandstone. It should be pointed out that the pore pressure for the Bandera Sandstone was maintained at 1.6 MPa, while for the Berea Sandstone specimen was kept at 2.5 MPa. The initial compressibility value for the manufactured sandstone, measured at 5 MPa effective confining stress, lies within the values from both natural rocks and the trend of the line starts to reach a plateau behavior at around 20 MPa of confining pressure.

5 CHAPTER 5 WETTABILITY

5.1 Introduction

Wettability is the property that describes the preference of a solid material (reservoir rocks) to be in contact with one fluid rather than other (oil, water or gas). These forces greatly influence the hydrocarbon reservoir behavior in many ways; playing an important role on the fluid saturation profile, log interpretation parameters, multiphase flow and ultimately, oil recovery (i.e. productivity). Understanding the wettability of the productive formations of a reservoir is essential to understand and predict the reservoir performance and design any particular enhanced oil recovery (EOR) campaign that might be applied during the project. It is important to note that in many oilfield applications, wettability is treated as a "binary switch" and this generalization cloaks the complexity of wetting physics in a reservoir rock (Abdallah et al. 2007). During the experiments performed on 3D printed analogues, the fact that wettability is a "continuum" phenomenon will be clear as the printed cores will be catalogued as a mixed-wet material.

To analyze and study the wettability behavior of the 3D printed reservoir sandstone analogues, a quantitative test: contact angle measurement and qualitative tests: co-current imbibition and counter-current imbibition were performed using Amott cells (Anderson 1988). The contact angle test, as its name might indicate, relies on the measurement of the angle formed by a drop of fluid and the surface of a solid material, in presence of another fluid (i.e. air). Conversely, either the co-current or the counter-current imbibition tests are based on the volume of fluid spontaneously imbibed by a porous material. The test is considered finished when the fluid imbibition with time reaches a plateau behavior.

Analogous to the behavior observed by (Yassin et al. 2016) on the pore network of unconventional rocks as gas shales, the 3D printed cores exhibit a mixed-wet behavior in which parts of the rock surfaces are strongly oil-wetted and parts are water-wetted (Salathiel 1973). This can be explained by the fact that the manufactured specimens generally consists of an organic part (Furan binder) that is strongly oil-wet and preferentially imbibes the oleic phase

and of an inorganic part (Silica sand), which is well-known to be strongly water-wet and is preferentially hydrophilic.

5.2 Measurement of the Contact Angle

Contact angle measurements performed in contact with air (i.e. surrounding atmosphere conditions) were performed with the purpose of computing the wettability of the isolated furan binder and the fresh sandstone analogues. A thin section (approximately 1 mm) of Furan Binder mixed with acidic activator at a volume proportion of 0.1% volume of acid to furan alcohol was placed onto a glass sample holder and it was left curing under ambient temperature until it was completely solid.

Additionally, two disks of 38.1 mm diameter by 10 mm thickness (1.5 in. by 0.39 in.) were printed using three different configurations: B10.O90.T250 and B20.O90.T250. The surface used to perform the experiment was carefully polished to diminish its roughness and therefore reduce the hysteresis on the contact-angle measurements.

Using a Video Contact Angle (VCA) equipped with a heated syringe assembly, various drops of distilled water and silicone oil were placed on top of both the solidified binder and the 3D polished-disks to measure three-phase contact angle with each surface. At the same time, using a precision camera, it was possible to capture high-resolution images of the test fluid-surface interaction and to determine the tangent lines for the basis of the contact-angle measurement (Optima 2017). Once the equilibrium was reached, the final oil/water shape was recorded.

The contact angle of the pure furan binder was measured in presence of water and silicone oil. The results for both fluids are presented in Figure 5.1. Left and right measurements of the contact angle are presented at the bottom of the image; an average angle of 96.1 degrees was obtained when measuring the contact angle with water, whereas 21.8 degrees was obtained when placing the drop of oil on top of the surface. This study shows the clear preference of the Furan to be wetted by the silicone oil. However, the preference of the 3D printed specimens for any of the previous fluids has to be addressed specifically since the affinity of the silica sand to water has been clearly recognized from previous experience. For this reason, the wettability of

the sandstone analogues can be highly influenced by either the amount of organic components (i.e. volume of Furan) or the volume of oil-repellent compounds (i.e. Silica Sand grains).

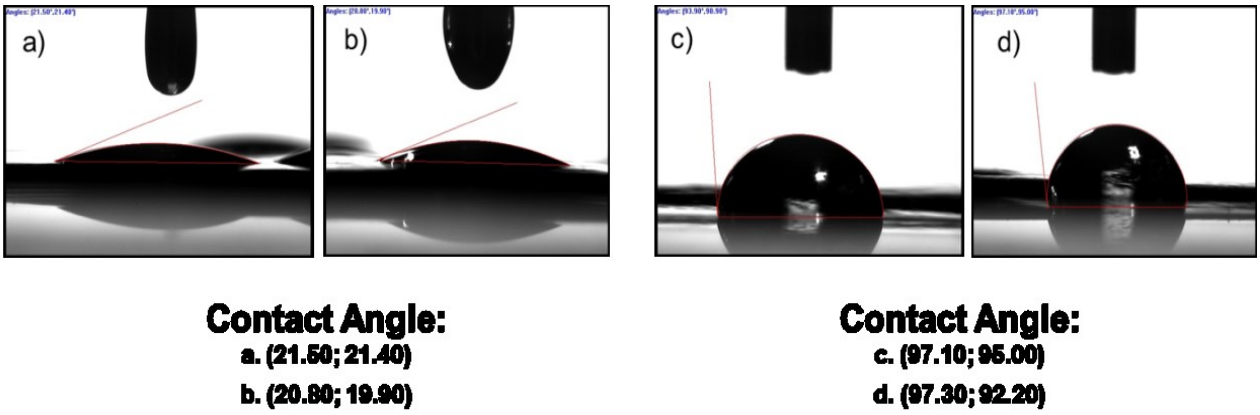

Figure 5.1 Measurement of the Contact Angle at the Binder Surface with a & b) Oil and c&d) Water

The wetting affinity of the fresh 3D printed specimens or green cylinders (named like that for its initial color) in the presence of water (air/water) and oil (air/oil) was also measured. The oil droplet placed on top of each disc, regardless its printing configuration, was totally spread on the sandstone surface. Contrary to this behavior, the water droplet formed a measurable contact angle on the rock of the surface. Figure 5.2 and Figure 5.3 show the measurement of the contact angle using water as the wetting fluid in specimens printed with 10% and 20% binder saturation respectively.

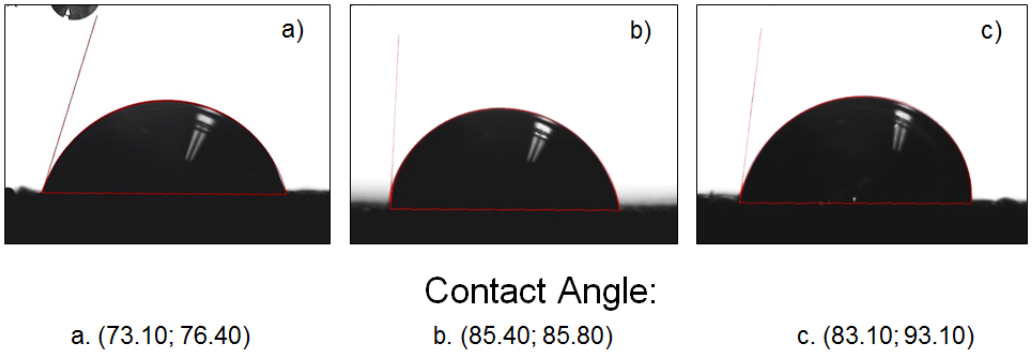

Figure 5.2 Measurement of the contact angle at the 3D printed sandstone surface printed with 10% binder saturation

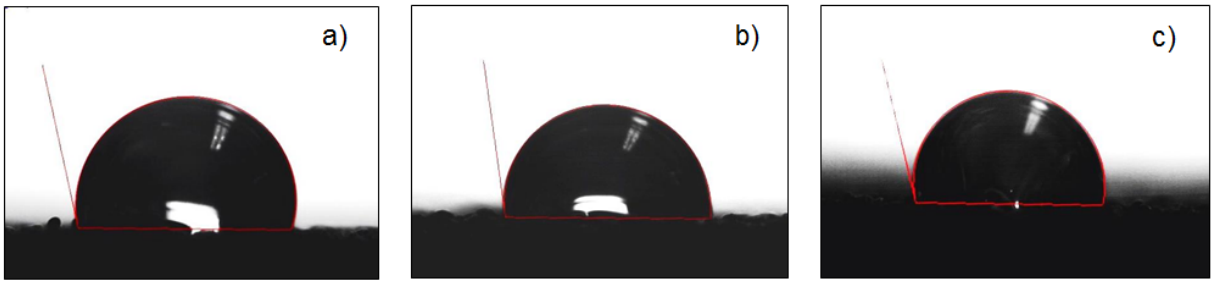

Figure 5.3 Measurement of the contact angle at the 3D printed sandstone surface printed with 20% binder saturation

On average, as shown in Figure 5.2, the contact angle for specimens printed with 10% binder saturation is 82.8, indicating a hydrophilic material. For samples printed with 20% binder saturation the average contact angle was 101.4 as shown in Figure 5.3. Results of this testing phase suggest that the 3D printed material becomes more hydrophobic when the amount of binder placed in the specimens during its construction is increased. Table 5.1 summarizes all the measured values of contact angles for oil and water in the furan's surface and in the 3D printed specimen's surface.

Table 5.1 Air/Water and Air/Oil Contact Angle Measurement.

Material	Contact Angle	
	Oil	**Water**
Furan Binder-S1	21.45º	96.05º
Furan Binder-S2	20.35º	94.75º
B10.O90.T250-1	0º	74.75º
B10.O90.T250-2	0º	85.6º
B10.O90.T250-3	0º	88.1º
B20.O90.T250-1	0º	104.5º

B20.O90.T250-2	0º	96.5º
B20.O90.T250-3	0º	103º

5.2.1 Contact Angle on Saturated Specimens

Two different combinations of fluid-rock systems were also analyzed. First, cores printed with 10% binder saturation were immersed into water/oil until reaching 100% saturation. Two droplets, one of water and other of oil were placed on top of the saturated cores and the contact angle was measured. Second, one specimen saturated with water and other one saturated with oil were submerged at the same time into two different containers full of silicone oil. After the whole system was considered to be steady, one droplet of tap water was placed into each one of the containers and the contact angle with the surface of both 3D printed analogues was measured.

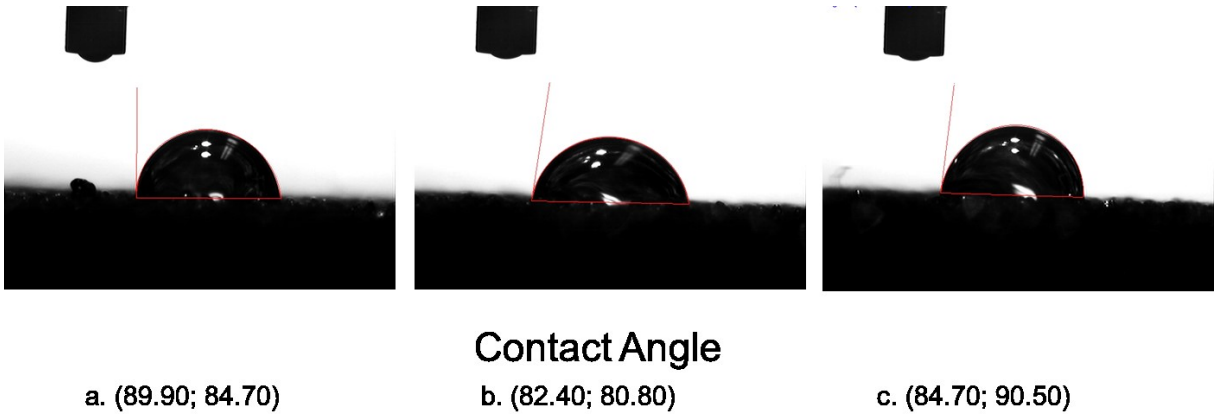

Figure 5.4 Measurement of the Contact Angle at Oil Saturated Sepcimens

The effect of soaking the samples in water and oil are summarized on Table 5.2. For the case of the water-saturated core, both water and oil droplets placed on its surface were immediately spread onto the rock surface. This decrease on the water contact angle may indicate that aging in water increases the affinity of the 3D printed analogues to this fluid. However, the affinity

of this material to oil remains unaffected (i.e. contact angle did not changed with respect to the freshly-printed cores). For the case of the silicone oil-saturated specimen, the oil droplet spreads onto the rock surface whereas the water droplet slightly increased its contact angle by around 4%, with respect to the green cylinders.

Table 5.2 Measurement of contact angle in saturated cores

	Contact Angle			
Surrounding fluid	**Air**			
Saturating Fluid	**Water**		**Oil**	
Droplet	Oil	Water	Oil	Water
Sample 1	0	0	0	87.3
Sample 2	0	0	0	81.6
Sample 3	0	0	0	87.6

Testing thus far involves contact angles of water/oil with the 3D printed rock surface surrounded by air. However, at reservoir conditions, the wettability of the rocks is highly influenced by the predominant pore fluids encountered within this media (reservoir water/brine and oil). Additionally, contact agles are much lower in the presence of air than in presence of oil (Wei et al. 1993). Therefore, it is important to investigate the possible effects of the surrounding fluid (distilled water/ silicone oil) on the wettability and surface interaction of the sandstone analogues' surface.

Results for the oil/water-saturated specimens submerged in silicone oil are presented in Figure 5.5 and Figure 5.6. The images were captured once the droplet was stabilized and, in this case, the contact angle was measured using Image-Analyzer software. For the case of the silicone oil-saturated core, the tap water droplet exhibits a remarkable increment on the contact angle with respect to the results obtained on freshly-printed specimens. The exact value obtained under this scenario was an angle of 150°; as shown clearly in Figure 5.5. The fact that the core

was previously submerged and saturated with silicone oil, enhances the tendency of the 3D printed material to prefer being wetted by this fluid, showing a clear hydrophobic behavior.

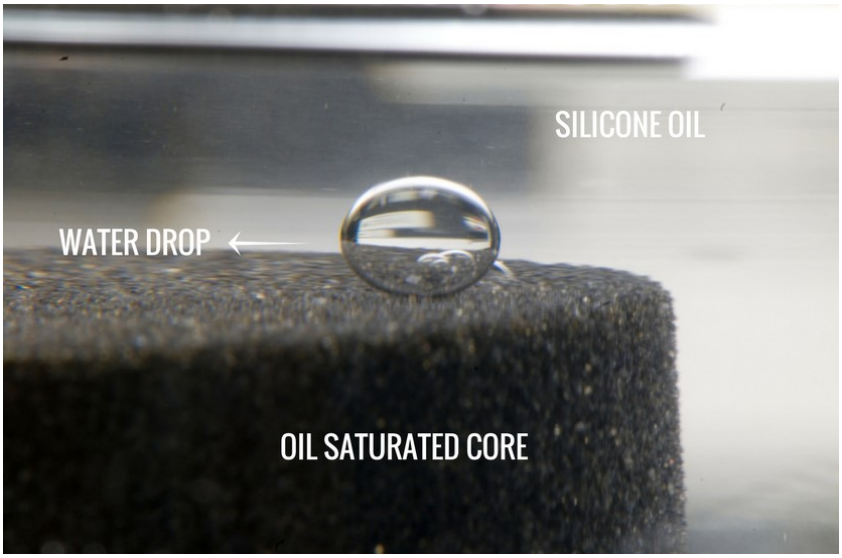

Figure 5.5 Contact angle measurement for oil-saturated cores submerged in silicone oil.

Figure 5.6 Contact angle measurement for water saturated cores submerged in silicone oil.

Referring to the water-saturated core submerged in silicone oil, the water droplet placed onto the container quickly spreads along the surface of the specimen, as shown by Figure 5.6**.** This behavior indicates a strong preference of the 3D printed material to be wetted by water when previously saturated by this fluid. Furthermore, there is a clear change in the printed sandstone

specimen's color with respect to a freshly printed specimen. In this case, the sample turns into a golden-brownish tone. Studies (Schmitt 1974) have shown that pure furfuryl alcohol is a colorless liquid that darkens rapidly to an amber color in the presence of air due to autoxidation. Apparently, even with thermal treatment this deterioration can not be retarded or avoided. In presence of water and air the 3D printed material oxidizes with time, gradually changing its color from a dark green color to a golden-brownish tone.

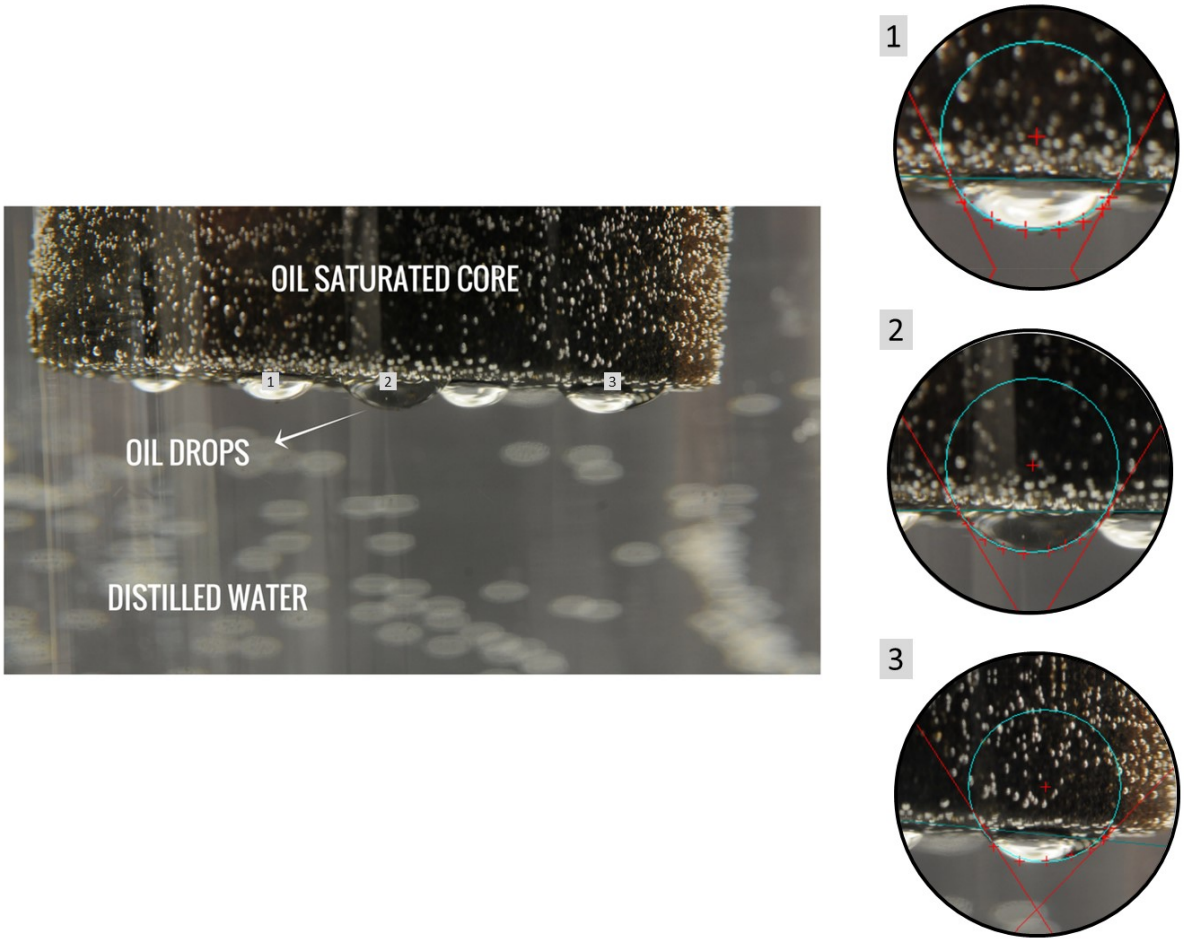

Figure 5.7 Contact angle measurement for oil saturated cores submerged in distilled water.

Figure 5.7 presents equilibrated droplets of silicone oil seating on the surface of an oil-saturated 3D printed core that is immersed in distilled water. The inset images in Figure 5.7 illustrates

the character of each oil droplet. Detailed image analysis on each drop using Surftens 4.7^{TM} software was used to find the real contact angle of the fluid with the surface of the printed specimen. The average contact angle in this case was 56.6°.

Figure 5.8, shows equilibrated droplets of silicone oil seating on the surface of a water-saturated 3D printed core that is immersed in distilled water. Contact angle results shows that the surface of the core is completely oleophobic. The average value measured was 156^{o}.

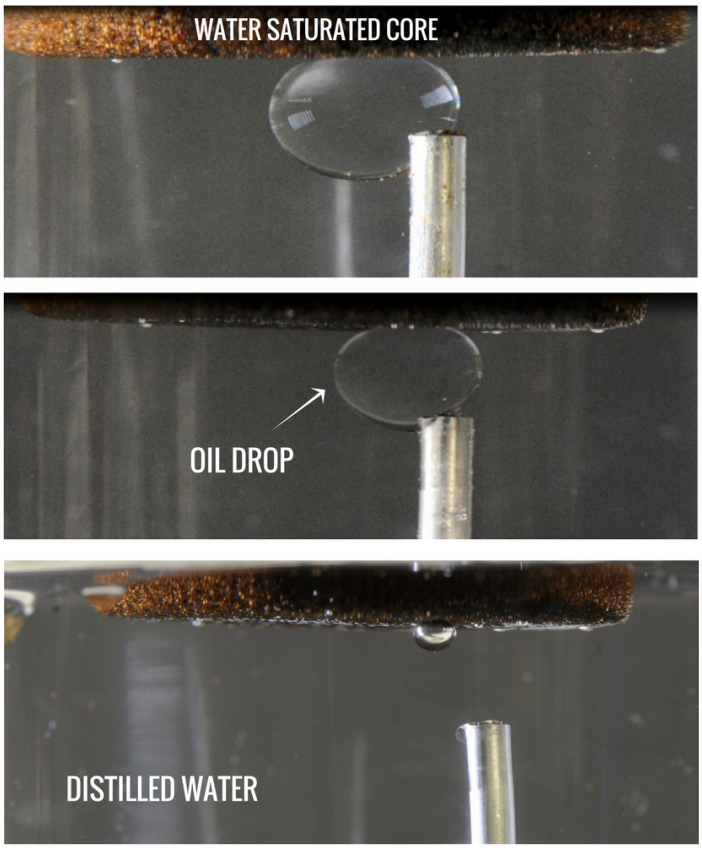

Figure 5.8 Contact angle measurement for water saturated cores submerged in distilled water.

The value of contact angle obtained for each droplet is presented in Table 5.3. The surrounding fluid on the table refers to the fluid that is around the specimen; the saturating fluid refers to the liquid that is in the pore space of the core; and the droplet stands for the type of fluid in the drop.

Table 5.3

	Contact Angle			
Surrounding fluid	**Oil**		**Water**	
Saturating Fluid	**Water**	**Oil**	**Water**	**Oil**
Droplet	**Water**	**Water**	**Oil**	**Oil**
Sample 1	0	162	157.9	59
Sample 2	0	148	153	59.4
Sample 3	0	159	156.5	51.5

5.3 Co-Current Spontaneous Imbibition on Fresh 3D Printed Analogues

In a co-current displacement the wetting and non-wetting fluids move in the same direction with the non-wetting phase being pushed out ahead of the wetting phase (Unsal et al. 2007). Co-current spontaneous imbibition of silicone oil and distilled water was measured into fresh (i.e unsaturated) 3D printed sandstone specimens. 24 cylinders of 38.1 mm diameter by 76.2 mm length (1.5 in. by 3 in.) were printed, from which 12 were manufactured using printing configuration B20.O90.T250, previously defined on Figure 3.4; to check the repeatability of the results. The remaining 12 analogues were created in order to determine the incidence of the printing configurations on the wettability. Thus, half of them were built using B10.O90.T250 configuration and the other half were printed with B30.O90.T250.

Prior to start the test, 12 identical replicas of a basic imbibition cell (Lan et al. 2015) were built for each specimen by fixing inside a sealed glass container a piece of metallic mesh on top of a circular plastic pedestal. Once the entire number of cells was ready to be used, half of the setups were filled with distilled water up to the level of the metallic mesh to assure that the cylinder will be in contact with the fluid just at the bottom end. The remaining cells were filled in the same manner with silicone oil. A schematic image of the configuration of the imbibition cells is shown in Figure 5.9. Before placing the 3D printed sand specimens inside the chambers, their initial weight was recorded using a high-resolution scale for the calculations of the imbibed volume along the test.

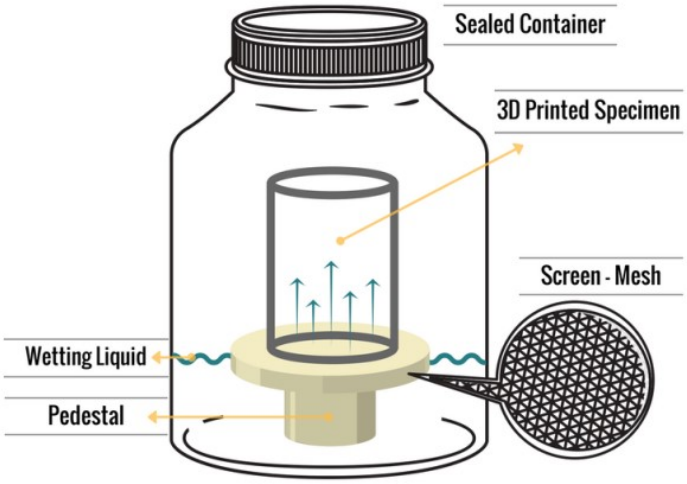

Figure 5.9 Schematic of the imbibition cell setup.

Figure 5.10, Figure 5.11 and Figure 5.12 show the results obtained in the co-current spontaneous imbibition tests. Once the tests started, the mass of fluid gained by each sample was periodically monitored and recorded for a period of 8 weeks, where the normalized imbibition volume with time reached a plateau. The volume of imbibed fluid was normalized by dividing the absorbed volume of silicone oil or water by the sample pore volume (Habibi et al 2016).

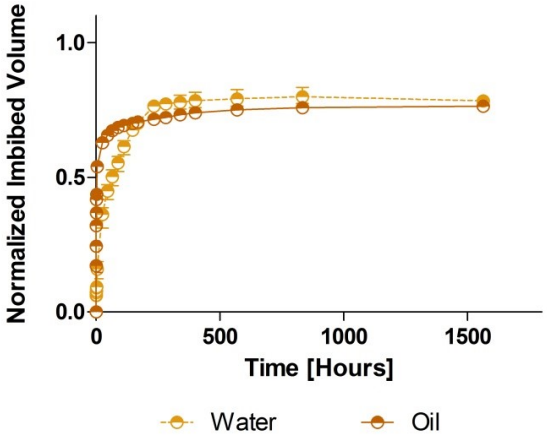

Figure 5.10 Normalized Imbibition Volume with Time for Cylinders Printed with 10% Binder Saturation

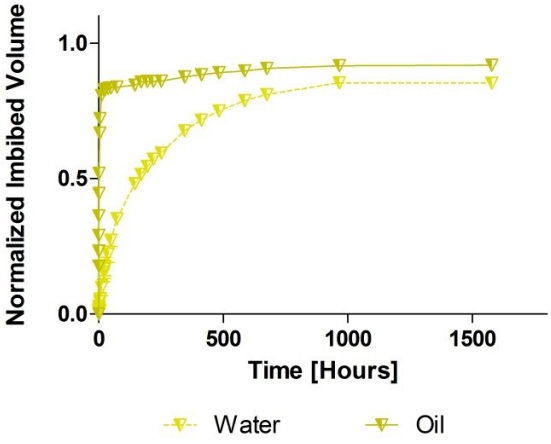

Figure 5.11 Normalized Imbibition Volume with Time for Cylinders Printed with 20% Binder Saturation

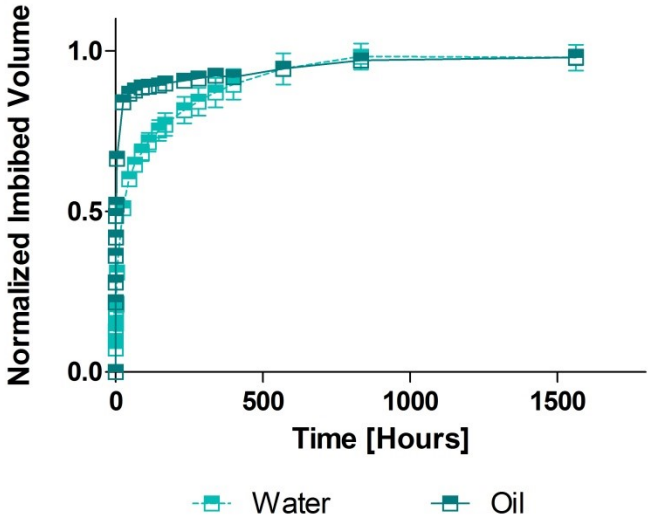

Figure 5.12 Normalized Imbibition Volume with Time for Cylinders Printed with 30% Binder Saturation

Figure 5.13 presents the data obtained from the spontaneous imbibition tests (water-air and silicone oil-air). The left side of the plot displays the individual comparison between the normalized volumes of both silicone oil and distilled water imbibed by each set of specimens grouped by their binder saturation. The right side of the figure summarizes the results by fluid, to facilitate the evaluation of the results. At the beginning of the experiment, for cylinders in contact with silicone oil, regardless of its binder saturation, the volume of fluid imbibed increased at a fast rate and then it increased gradually until reaching the equilibrium (i.e. plateau section).

The behavior of the imbibition process of the analogues in contact with water was slightly different; the rate of fluid intake was slower from the beginning than the rate of the specimens in contact with oil, however, once the imbibed volume reached the equilibrium, the amount of water imbibed was as much as the specimens in contact with silicone oil, regardless of their initial porosity. In fact, for the cylinders printed using 10% binder saturation, the volume of water imbibed at equilibrium was even higher than the volume of silicone oil imbibed by the specimens of this same configuration.

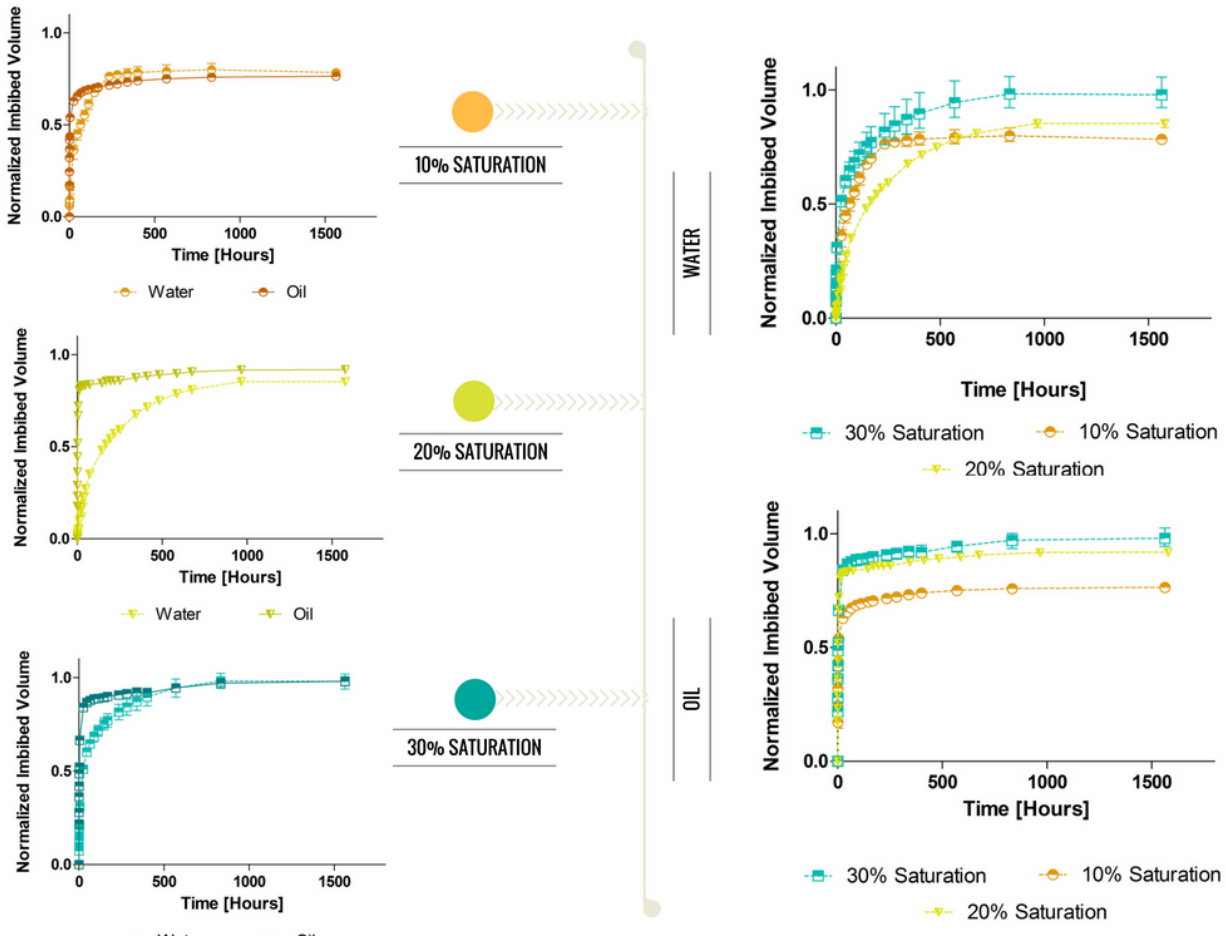

Figure 5.13 Summary of Normalized Imbibition Volume with Time plots

The fact that both silicone oil and distilled water spontaneously imbibe the 3D printed analogue's porous media against gravity, in presence of air, directly indicates the mixed-wet characteristics of this material (Lan et al. 2015). A stronger affinity to silicone oil from the specimens built with 20% and 30% saturation was observed during the experiments, while cylinders with 10% binder saturation displayed a less palpable oil-wet core. The explanation for this behavior is that the organic part (furan binder) preferentially imbibes the oleic phase. In contrast, the inorganic part is usually hydrophilic and preferentially imbibes the aqueous phase (Yassin et al.2016).

The results obtained in this stage of the experiment, were in accordance with those presented by Li et al 2015, where it was concluded that the smaller the effective capillary radius, in this

case the pore size diameter, the shorter the time needed to approach the same imbibed weight. This can be evidenced with the shorter time required by the specimens with 20% binder saturation to imbibe almost 70% of the void space of the analogue with silicone oil, compared with the cylinders printed with 10% saturation, which spontaneously imbibed around 60%.

5.4 Counter-Current Spontaneous Imbibition on Saturated Specimens

Once the spontaneous imbibition on fresh specimens was concluded, the cylinders saturated with silicone oil were placed in an Amott imbibition cell filled with distilled water. The exact configuration of the imbibition cell is shown in Figure 5.14. This cell allows silicone oil/water displaced by distilled water/silicone oil to be collected and measured at the top of the imbibition cell. Both imbibition cells were sealed to avoid any liquid evaporation to the atmosphere (i.e. there is no change of fluid mass throughout the duration of the experiment).

The design does not differ from the original qualitative method for determining the degree of water/oil wetness of a rock proposed originally by Anderson (1988). This method is suitable for an initial characterization of 3D printed sandstone analogues because it offers a rapid indication about the wettability of a specific material without the requirement of sophisticated equipment. Nonetheless, the estimation obtained by this technique is influenced by fluid viscosity, pore structure and initial saturation conditions; thus, a quantitative (i.e. precise estimation) method is required to accurately investigate this property.

The counter-current imbibition experiments performed on saturated cores over a period of 33 days appears to demonstrate that the 3D printed analogues are neutrally wet (Anderson 1988). The oil-saturated cores that were placed in water, did not experience any pore fluid displacement by means of the surrounding fluid. An analogue behavior was exhibited by the water-saturated cores. The fact that the pore fluid was completely retained by the specimen is because the gravity forces or capillary pressures were insufficient to overcome the capillary entry pressure. Therefore, nor free drainage or capillary displacement occurred (Schechter et al. 1994). This behavior shows the preference of this material for both fluids, water and silicone oil.

Figure 5.14 Water and Silicone Oil Saturated Specimens immersed in Silicone Oil and Water Respectively.

However, after 33 days, a small amount of oil and water was collected at the top and bottom of the Amott cells, respectively. The cores were left for 40 more days with the purpose of monitoring the amount of fluid collected in the cells. After 75 days of imbibition, the test was concluded. The final results are summarized in Figure 5.15. In both cases, the amount of expelled fluid is small, for the oil-saturated cores, around 0.4 mL of silicone oil on the first and around 0.2 mL on the second came out from the specimens, while for the water-saturated cores, around 0.2 mL of blue-colored tap water were expelled from the sample (the water was tinted using a droplet of vegetable blue dye. As the amount of dye was so small, there is no change on the water's surficial tension).

Even though the amount of wetting fluid (either water or silicone oil) expelled from the 3D printed specimens was not a substantial volume (0.4 mL, which was the maximum volume of wetting fluid collected corresponds just to 1.2% of the 20%-binder saturation analogue's total pore volume), it is sufficient to support the conclusion that the sandstone analogues are a mixed-wet material (i.e. a material with inhomogeneous wetting preferences, which can include intermediate-wetting). These results are, at the same time, in accordance to the results obtained from the co-current imbibition experiments.

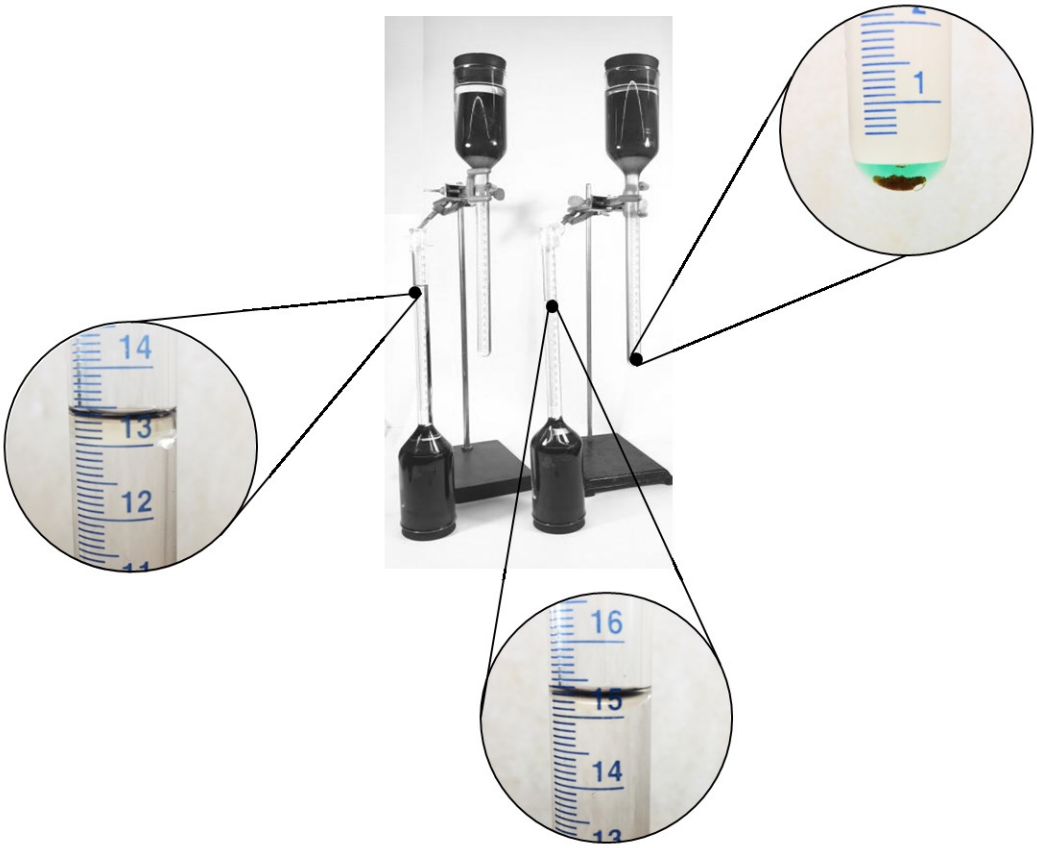

Figure 5.15 Counter-Current imbibition test after 60 days

6 CHAPTER 6 MERCURY INTRUSION CAPILLARY PRESSURE TEST

6.1 Introduction

Mercury intrusion capillary pressure (MICP) measurement is a standard destructive method that facilitates the interpretation of size and geometry of rock's pores and throats. Since AM allows the manufacturing of a great number of samples, multiple samples is not a limitation for destructive testing; therefore the implementation of this technology is not a concern due to the availability of specimens.

Mercury, which is a non-wetting fluid, enters the pore space when pressure is applied. As pressure is increased, mercury progressively invades smaller spaces and, providing a sufficiently high pressure, the pore system becomes saturated (Wardlaw and Taylor 1976). Once the pressure reaches the upper limit, the extrusion process begins, while pressure is decreased incrementally to atmospheric pressure (Elgmati et al. 2011). Results obtained from these tests allow the determination of different parameters that are of great importance in the characterization of the rock matrix. For instance, capillary pressures, first introduced by (Purcell 1949), porosity and pore size distribution are some of the properties that can be analyzed and described with MICP test.

Several MICP tests were performed on 3D printed sandstone analogues printed over all printing configurations considered in this research. Results for capillary pressure, porosity and pores size distribution suggest the following:

1. The entire combination of arrangements printed exhibited that the range of values obtained and the shape of the curves were reasonably similar. Mercury capillary pressure curves are dependent upon the pore size distribution and tightness, rock and fluid type, and saturation history (Elgmati et al. 2011). The fact that all capillary pressure curves ended up being similar suggest analogous and homogeneous rock matrices since the fluid and saturation history were kept constant;
2. Porosity which is a fundamental property and is function of the bulk volume and pore volume, showed an increase in the pore space when decreasing the binder saturation; and

3. Pore size distribution is mainly referred to as pore-throat size and it is defined as the pore size that connects the larger pores. It is based on the concept that inter-particle pore space can be visualized as rooms with connecting doors. The doors are the pore-throats that connect the larger pores, or rooms (Lucia 2007). The range of pore size distribution obtained with MICP test is 30 to 80 μm, suggesting that the pore structure of the 3D printed specimens is mainly conformed by nodal big pores.

6.2 Imbibition and Pore Size Distribution

For the complete set of samples, most of the mercury volume intrusion took place below atmospheric pressure; consequently, it was not possible to obtain a complete extrusion or drainage curve. Analyzing Figure 6.1, Figure 6.2 and Figure 6.3, a complete saturation underneath the atmospheric pressure is equivalent to a pore throat diameter of 30 to 90 μm, suggesting that the pore structure of the 3D printed specimens is mainly conformed by nodal big pores. Also, compared with the results obtained by Dastidar et al. (2007), it is possible to argue that the shape of the curves indicates a well sorted sample with a narrow pore size distribution. Figure 6.1 presents mercury intrusion curves varying the binder saturation alongside the equivalent pore diameter curve, which was calculated using Washburn equation (Washburn 1921):

$$D = \frac{-4\sigma \cos\theta}{P_c} \tag{6.1}$$

In this expression, P_c is the capillary pressure that must be applied to nonwetting liquid (mercury) to penetrate cylindrical pores of diameter D, and σ and θ are the mercury's surface tension and contact angle, respectively. For this set of samples, the average pore diameter was determined to be 58.3 μm, 51.7 μm and 57.9 μm for 10%, 15% and 20% binder saturation, respectively. Pore throat diameter was calculated using Equation 6.1 with a contact angle of 130° and a mercury surface tension of 486 dynes/cm.

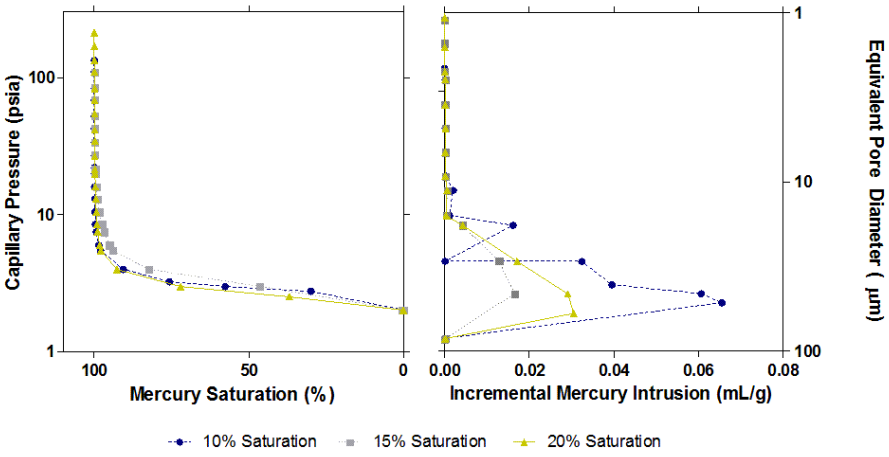

Figure 6.1 Imbibition Curve for Mercury Intrusion Capillary Pressure Test on 3D Printed Sandstones with Different Binder Saturation and their Equivalent Pore Size Distribution Curve

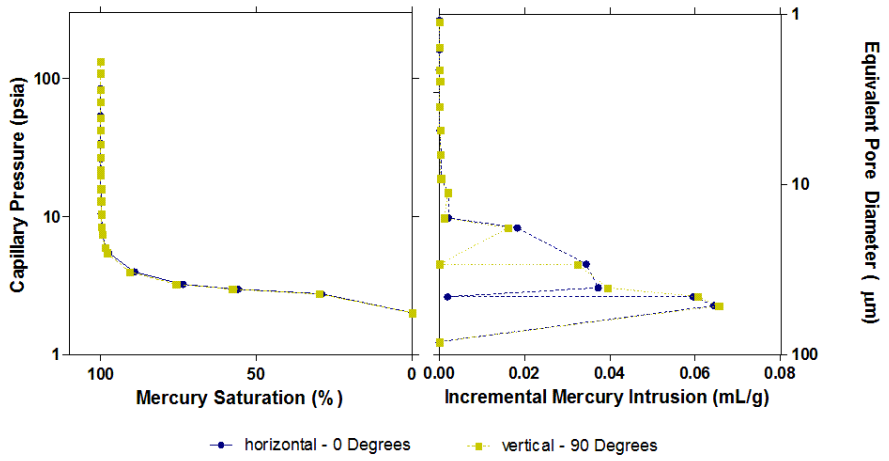

Figure 6.2 Imbibition Curve for Mercury Intrusion Capillary Pressure Test on 3D Printed Sandstones with Different Layer Orientations and their Equivalent Pore Size Distribution Curve

Figure 6.2 shows mercury intrusion curves alongside the equivalent pore diameter curve; in this case, the analysis is focused on the variation of the printing-layer orientations explored for the study. Both vertical (90°-inclined layers) and horizontal (0°-inclined layers) specimens exhibit a nearly analogous behavior, substantial portion of the incremental mercury intrusion and nearly 100% of the pore volume saturation is achieved under 10 psia, suggesting that there is no significant difference in the pore structure when varying the orientation of the printed samples. On the other hand, as shown in Figure 6.3, variations on silica sand's layer thickness, is causing a slight change in the pore structure of the cylinders. Even though all of them present the same

range of pore size diameters, 400µm-layer thickness' specimens show a significant peak of mercury intrusion at around 5 psia, suggesting a substantial amount of 80 µm pores, whereas the mercury intrusion for 600-layer thickness indicates smaller pores and more uniform distribution of pore size diameters.

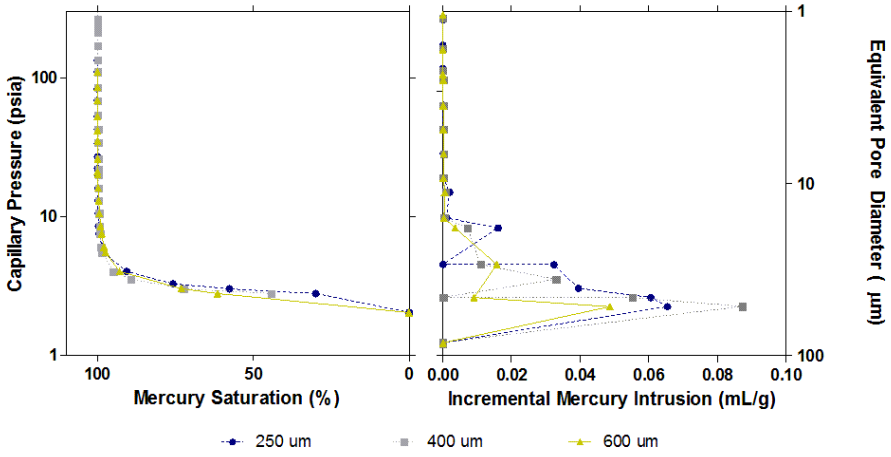

Figure 6.3 Imbibition Curve for Mercury Intrusion Capillary Pressure Test on 3D Printed Sandstones with Different Layer Thickness and their Equivalent Pore Size Distribution Curve

6.3 Porosity and Average Pore Diameter

A specimen's porosity can be indirectly calculated from the results obtained from an MICP test. Table 6.1 summarizes the different configurations that were printed with its corresponding calculated porosity. From these results, it could be inferred that the porosity has an indirect relationship with respect to binder saturation, a decrease of 25% on analogue's porosity when increasing furan saturation from 10% to 20%. This was an expected outcome as per binder saturation's definition, on which the actual furan volume, expressed in percentage of the specimen's total bulk volume, corresponds to the amount of void space that is being filled by the cured resin. Revil et al. (2014) studied 69 cores of Fontainebleau sandstone and found a porosity range of 5.4% to 19.4%. It is clear the 3D printed specimens display much higher porosities than natural sandstone, such as Fontainebleau. These results suggest that it will be appropriate to investigate methods for altering the packing ratio of the actual deposited sand

layer in the M-Flex, such as bed vibration or mechanical compaction, with the objective of reducing the high void space within the printed specimen.

Layer thickness and layer orientation, in contrast, does not appear to have any major influence in this property. Nonetheless, as shown in

Table 6.1, when printing with a layer thickness of 600µm, the porosity percentage reduction is 13%, compared with the base case (i.e. B10.O0.T250). The most reliable hypothesis considered to explain this behavior, in conjunction with the presence of smaller nodal pores, previously shown in Figure 6.3, is that, as the volume of sand that is placed into the print bed per recoat is increased, the influence of gravity on the re-organization of the grains of each newly-deposited layer is also enlarged. This phenomenon might generate a different packing rate in the overall volume of the specimens printed under this feature, producing a reduction on the bulk void space of the sample and at the same time, smaller pore diameters, on average.

Table 6.1 Porosity and Average Pore Diameter for Different 3D Printed Configurations

Specimen	Interstitial Porosity (Fraction)	Average Pore Diameter (µm)
B10.O0.T250	**0.476**	**57.47**
B10.O90.T250	**0.476**	**58.29**
B15.O90.T250	**0.37**	**51.69**
B20.O90.T250	**0.357**	**60.34**
B10.O90.T400	**0.476**	**57.88**
B10.O90.T600	**0.414**	**62.31**

7 CHAPTER 7 CONCLUSION AND RECOMMENDATIONS

7.1 Summary

The accurate modeling of production performance and recovery processes in petroleum and gas reservoirs is heavily influenced by the heterogeneity of natural geomaterials. The reliability of these studies on the accurate estimation of the hydraulic properties of the reservoir rock stratum constitutes a challenging condition to be handled by the implementation of additive manufacturing processes. 3D printing techniques will provide to the researchers the ability of ensuring the repeatability of petrophysical and flux properties determined by experimental processes in laboratory. The scope of this research includes a complete comprehensive analysis of the influence of printing configuration and features to determine whether, and in which manner, these variables influence the resulting hydraulic properties of the rock analogues to be fabricated.

This dissertation focuses on the characterization of hydraulic properties of the 3D printed sandstones analogues such as, porosity, wettability and permeability. Moreover this study provides a sufficient insight on the impact of specimen print configurations on sample's anisotropy and flow properties. Finally, the results obtained by the testing campaign are compared with those existing from the literature for natural sandstones such as Berea and Fontainebleau sand formations. The most important results are:

- By analyzing the trend of the uniaxial confining stress peak strength of specimens saturated with oil and water and their exposure time, it was possible to confirm whether the sandstone analogues were having any strength or structural affectation that might generate an anisotropic volumetric behavior when subjected to the planned effective confining stress levels during permeability tests. Results showed that for the cylinders submerged in water, the UCS peak strength was reduced by an average of 42% with respect to the unsaturated case (i.e. base case), whereas for the specimens submerged in silicone oil, UCS peak strength was reduced by an average of 5%.

- The orientation of the building planes has almost no clear influence on the permeability of the analogues. Contrary to the results obtained by several; where heterogeneous rock permeability values generated by the presence and orientation of either bedding planes or lamination with respect to the experimental flow direction, on natural sandstones, implied a variation on the measured fluid velocity (Darcy Flow) and hence on the permeability measurements. Nonetheless, results obtained in specimens with 10% saturation, independently of the layer orientation, show an appreciable irreversible deformation as the effective confining stress is increased above 5 MPa. This effect is clearly evidenced with a notable reduction of the specimens' permeability, represented by a steeper declining trend of the slope after reaching this stress value. In addition, a significant hysteresis of the plot is shown during the unloading portion of the curve, it could be noted that the magnitude of the permeability's decrement is no longer recovered, even after almost achieving the initial stress conditions. A minor recovery on the permeability value was exhibited once the effective confining stress was reduced to 1.0 MPa.

- Results obtained from SEM and OM show physical evidence of a structural variation in the pore space of the samples when varying the effective confining stresses. In fact, there is a change in the grain structure evidenced by the rearrangement of the grains, which tend to form clusters of particles in specific zones as a result of the anisotropic distribution the compacting stress throughout the body of the specimen.

- The variation of permeability when increasing the amount of binder placed into the sample (i.e. Binder Saturation) is remarkable. Specimens built up with 20% furan saturation showed an average permeability of 1,046 mD, which implies a 42.8% reduction in their initial permeability when compared to the 10%-saturation's specimens, with an average value of 1,833 mD. However, once the specimens are subjected to a higher level of effective confining stress reached throughout the test (10 MPa), 20%-saturation samples reach a maximum average permeability reduction of 27%, comparing the initial (freshly-printed) and final (after compaction) values; whereas for 10%-saturation specimens, the average percentage reduction observed was

55%. This behavior suggests that the cylinders manufactured using 10% furan saturation is more sensible to stress changes than those of 20% saturation. Specimens printed with 30% binder saturation highly differ one to the other one. The high range shown in the permeability vs effective confining stress curve show that the repeatability of the specimens when printing with this amount of binder saturation cannot be assured. The increased volume of furan that is sprayed by the printing head to build the 30% saturation specimens, a binder-saturation gradient could have been generated along the body of the specimens, which will induce the existence of highly-impregnated zones as well as poorly-saturated ones and therefore heterogeneous induced pressure gradient, which influences the permeability calculations, and low repeatability of the results.

- The contact angle of the pure furan binder was measured in presence of water and silicone oil. An average angle of 96.1 degrees was obtained when measuring the contact angle with water, whereas 21.8 degrees was obtained when placing the drop of oil on top of the surface. This study evidences the preference of the Furan to be wetted by the silicone oil. However, the preference of the 3D printed specimens for any of the previous fluids has to be addressed specifically since the affinity of the silica sand to water has been clearly recognized from previous experience. For this reason, the contact angle of the specimens was also calculated. Specimens printed with 10% binder saturation showed a contact angle of 82.8, indicating a hydrophilic material. For samples printed with 20% binder saturation the average contact angle was 101.4. Results of this testing phase, suggest that the 3D printed material becomes more hydrophobic when the amount of binder placed on the specimens during its construction is increased.

- Co-Current imbibition experiments showed that both silicone oil and distilled water spontaneously imbibe the 3D printed analogue's porous media against gravity, in presence of air. This behavior indicates the mixed-wet characteristics of this material. A stronger affinity to silicone oil from the specimens built with 20% and 30% saturation was observed during the experiments, while cylinders with 10% binder saturation displayed a less palpable oil-wet core. The explanation for this behavior is that the

organic part (furan binder) preferentially imbibes the oleic phase. In contrast, the inorganic part is usually hydrophilic and preferentially imbibes the aqueous phase.

- Counter-Current imbibition tests showed that after 75 days of experiment the amount of expelled fluid, for both specimens saturated with silicone oil and distilled water, was small, for the oil-saturated cores, around 0.4 mL of silicone oil on the first and around 0.2 mL on the second came out from the specimens, while for the water-saturated cores, around 0.2 mL of blue-colored tap water were expelled from the sample (the water was tinctured using a droplet of vegetable blue dye. As the amount of dye was so small, there is no change on the water's surficial tension).This behavior supports the conclusion that the sandstone analogues are a mixed-wet material (i.e. a material with inhomogeneous wetting preferences, which can include intermediate-wetting). These results are, at the same time, in accordance to the results obtained from the co-current imbibition experiments.

- Mercury intrusion capillary pressure (MICP) test was also performed in 3D printed specimens. For the complete set of samples, most of the mercury volume intrusion took place below atmospheric pressure; these results suggest a pore throat diameter of 30 to 90 μm, indicating that the pore structure of the 3D printed specimens is mainly conformed by nodal big pores. Also, it is possible to argue that the shape of the curves indicates a well sorted sample with a narrow pore size distribution

- The variation of the printing-layer orientations point out that, both vertical (90°-inclined layers) and horizontal (0°-inclined layers) specimens exhibit a nearly analogous behavior, where there is no significant difference in the pore structure when varying the orientation of the printed samples. On the other hand, variations on silica sand's layer thickness, is causing a slight change in the pore structure of the cylinders. Even though all of them present the same range of pore size diameters, 400μm-layer thickness' specimens show a significant peak of mercury intrusion at around 5 psia, suggesting a substantial amount of 80 μm pores, whereas the mercury intrusion for 600-layer thickness indicates smaller pores and more uniform distribution of pore size diameters.

- Specimen's porosity was indirectly calculated from the results presented on the MICP test. From these results, it could be inferred that the porosity has an indirect relationship with respect to binder saturation, a decrease of 25% on analogue's porosity when increasing furan saturation from 10% to 20%. Revil et al. 2014 studied 69 cores of Fontainebleau sandstone and found a porosity range of 5.4% to 19.4%. When comparing these results with the ones obtained on the porosity of 3D sandstone analogues, there is an increase of 145.3% on the upper case. These findings leads to contemplate those methods for altering the packing ratio of the actual deposited sand layer, as bed vibration or mechanical compaction, may be studied with the purpose of reducing the high void space within the specimen's body. Layer thickness and layer orientation, in contrast, does not appear to have any major influence in this property. Nonetheless, when printing with a layer thickness of 600µm, the porosity percentage reduction is 13%, compared with the base case (i.e. B10.O0.T250).

7.2 Conclusions

3D printed sandstone analogues built using silica sand and furan binders have proof to be a defensible material to replicate the porous media and transport properties of natural reservoir rocks. The ability of AM technology of building as many identical specimens as required for any research purpose, combined with the possibility of controlling their physical properties by varying the printing features used during their manufacturing process, makes 3D printing a suitable solution to design a limitless set of experiments that could overcome issues related to pore-structure repeatability or variability, scaling up and sample heterogeneity.

Nonetheless, there still exist some discrepancies on the range of values encountered for 3D printed materials compared with the properties of natural reservoir rocks. Permeability of sandstone analogues varies among 1.8 D and 2.0 D for calculated porosities encountered within 35.7% and 46.7%. Natural rocks as Berea sandstone normally have a permeability that ranges between 0.114 D to 1.168 D with porosities that oscillates between 19% and 26%. Simplifying the previously presented data, a direct comparison between natural and manufactured materials implies an increase of 41.6% on permeability values and of 44.3% on porosity.

With the purpose of fully understanding the influence of the manufacturing process on the sample's properties and aiming to close the gap between the behavior of sandstone analogues with natural materials, several printing features including binder saturation, layer orientation and layer thickness were selectively variated throughout the course of this research work. Binder saturation was demonstrated to negatively influence both specimen's permeability and porosity, this is to say, the higher the furan volume inside the sample, the lower the permeability and porosity values. Matching these findings with previous work related to 3D printed analogue's mechanical properties, furan saturation appears to fulfill all the requirements for building actual stronger material: elevating its peak strength and decreasing the value of its transport properties. With respect to pore size distribution, the incremental mercury intrusion of 10% saturation samples (i.e. specimens with the lowest binder content) was found to be remarkably influenced by large diameter pores (70-80 microns) and showed a wider range of pore sizes; porous media from 15% and 20% saturation specimens' curves exhibit an appreciable mercury intrusion just from pores higher than about 40 microns.

Finally, layer orientation appeared to not have an appreciable influence either on permeability or porosity of sandstone analogues. As suggested previously on the 'results' section, to fully understand the influence of non-homogeneities on 3D printed sandstone's transport properties, a functional and repeatable pore structure must be built and tested under various stress and fluid saturation conditions. Regarding printing-layer thickness, specimen's porosity was reduced on 13% just on 600-microns samples, while 400-microns specimens exhibited the same porosity as base case (250 microns). Pore size distribution from all cases has an equivalent shape and their incremental mercury intrusion is dominated by large diameter pores.

Contact angle of the specimens was measured with water. Specimens printed with 10% binder saturation showed a contact angle of 82.8, indicating a hydrophilic material. For samples printed with 20% binder saturation the average contact angle was 101.4. Results of this testing phase, suggest that the 3D printed material becomes more hydrophobic when the amount of binder placed on the specimens during its construction is increased. Nonetheless, spontaneous imbibition experiments using distilled water and silicone oil suggest that the 3D printed specimens are a mixed-wet material.

7.3 Recommendations and Future Work

Relative permeability tests should be carried out to determine the relative permeability vs. fluid saturation curves, which will contribute with highly valuable information to the analysis of the wettability behavior of the 3D printed sandstone analogues in presence of various fluids at the same time. Additionally, this type of tests will allow researchers to investigate the suitability of using manufactured sandstones as rock proxies to simulate waterflooding and fluid recovery tests on specific oil reservoirs.

The reduction of the porosity of the specimen is necessary to resemble in a more rigorous manner the properties of a reservoir rock. The high values of this property that the sandstone analogues possess at this stage of the project (26% for a 20%-binder saturation specimen) may influence the results obtained in fundamental properties as permeability and compressibility. Methods as the increment of the powder packing ratio by vibration or mechanical compaction are proposed to achieve this goal.

Forced imbibition wettability tests should be conducted to complete the drainage path of the capillary pressure vs. fluid saturation curves; this will allow the understanding of the interaction of the pore fluids with the surface of the 3D printed analogues and also to inspect in a more detailed manner the preference of the silica-furan structure to be in contact with a fluid.

The sensitivity of the silica-furan structure to water presents challenges when conducting flow tests. Research on alternate binder chemicals should be performed to find solutions to overcome this issue. Additionally, a chemical coat that prevents the oxidation of the specimens when sitting at ambient conditions will be desirable to avoid the degradation of the integrity of the specimens.

BIBLIOGRAPHY

"3D Printing Materials | ExOne." http://www.exone.com/Resources/Materials (June 29, 2017).

Abdallah, Wael et al. 2007. "Fundamentals of Wettability." *Oilfield Review*: 44–61. https://www.slb.com/~/media/Files/resources/oilfield_review/ors07/sum07/p44_61.pdf.

Anderson, William G. 1988. "Wettability Literature Survey- Part 2 : Wettability Measurement." *Petroleum Technology*.

Bak, David. 2003. "Rapid Prototyping or Rapid Production? 3D Printing Processes Move Industry towards the Latter." *Assembly Automation* 23(4): 340–45. http://www.emeraldinsight.com/doi/10.1108/01445150310501190.

Banks, Jim. 2013. "Adding Value in Additive Manufacturing: Researchers in the United Kingdom and Europe Look to 3D Printing for Customization." *IEEE Pulse* 4(6): 22–26.

Bassoli, Elena, Andrea Gatto, Luca Iuliano, and Maria Grazia Violante. 2007. "3D Printing Technique Applied to Rapid Casting." *Rapid Prototyping Journal* 13(3): 148–55. http://www.emeraldinsight.com/doi/10.1108/13552540710750898.

Berman, Barry. 2012. "3-D Printing: The New Industrial Revolution." *Business Horizons* 55(2): 155–62. http://dx.doi.org/10.1016/j.bushor.2011.11.003.

Bernabé, Y., U. Mok, and B. Evans. 2003. "Permeability-Porosity Relationships in Rocks Subjected to Various Evolution Processes." *Pure and Applied Geophysics* 160(5): 937–60.

Bose, Susmita, Sahar Vahabzadeh, and Amit Bandyopadhyay. 2013. "Bone Tissue Engineering Using 3D Printing." *Materials Today* 16(12): 496–504. http://dx.doi.org/10.1016/j.mattod.2013.11.017.

Campbell, Thomas, Christopher Williams, Olga Ivanova, and Banning Garrett. 2011. "Could 3D Printing Change the World?"

Chapwanya, Michael, and John M Stockie. 2010. "Numerical Simulations of Gravity-Driven

Fingering in Unsaturated Porous Media Using a Non-Equilibrium Model." *Water Resources Research an American Geophysical Union Journal* 46(9).

Churcher, P.L., P.R. French, J.C. Shaw, and L.L. Schramm. 1991. "Rock Properties of Berea Sandstone, Baker Dolomite, and Indiana Limestone." *Society of Petroleum Engineers*: 431–66. http://www.onepetro.org/mslib/app/Preview.do?paperNumber=00021044&societyCode=SPE%5Cnhttp://www.onepetro.org/doi/10.2118/21044-MS.

Corbett, P.W.M., P.S. Ringrose, J.L. Jensen, and K.S. Sorbie. 1992. "Laminated Clastic Reservoirs: The Interplay of Capillary Pressure and Sedimentary Architecture." *SPE Annual Technical Conference and Exhibition*. http://www.onepetro.org/doi/10.2118/24699-MS.

Cueto-Felgueroso and R. Juanes. 2009. "A Phase Field Model of Unsaturated Flow." *American Geophysical Union* 45(June): 1–23.

Dastidar, Rahul, Carl H Sondergeld, and Chandra S Rai. 2007. "An Improved Empir I Cal Per Me Abil Ity Esti Ma Tor from Mer Cury Injec Tion for Tight Clastic Rocks." *Petrophysics* 48(3): 186–90.

Ehrlich, R., Crabtree, S. J., K. O. Horkowitz, and J. P. Horkowitz. 1991. "Petrography and Reservoir Physics I: Objective Classification of Reservoir Porosity." *American Association of Petroleum Geologists Bulletin* 75(10): 1547–62.

Elgmati, Malek, Hao Zhang, Baojun Bai, and Ralph Flori. 2011. "Submicron-Pore Characterization of Shale Gas Plays." *SPE North American Unconventional Conference and Exhibition*: 1–19.

ExOne. 2009. *Safety Data Sheet*. 2014. "MFlex™_User_Manual_1.02.07_EN_US.pdf."

Farzadi, Arghavan, Mehran Solati-Hashjin, Mitra Asadi-Eydivand, and Noor Azuan Abu Osman. 2014. "Effect of Layer Thickness and Printing Orientation on Mechanical Properties and Dimensional Accuracy of 3D Printed Porous Samples for Bone Tissue Engineering." *PLoS ONE* 9(9): 1–14.

Fereshtenejad, Sayedalireza, and Jae Joon Song. 2016. “Fundamental Study on Applicability of Powder-Based 3D Printer for Physical Modeling in Rock Mechanics.” *Rock Mechanics and Rock Engineering* 49(6): 2065–74.

Gomez-Ramirez, J., Ardila, N., Chalaturnyk, R., Zambrano-Narvaez G. 2017. “Mechanical Properties Characterization of 3D Printed Sandstone Analogues Final draft(Rev2-March28) (Last Corrections).” : 23.

Gomez, Carmen T., Jack Dvorkin, and Tiziana Vanorio. 2010. “Laboratory Measurements of Porosity, Permeability, Resistivity, and Velocity on Fontainebleau Sandstones.” *Geophysics* 75(6): E191.

Habibi, Ali et al. 2016. “Advances in Understanding Wettability of Tight Oil Formations : A Montney Case Study.” In *SPE Annual Technical Conference and Exhibition*,.

Head, D., and T. Vanorio. 2016. “Effects of Changes in Rock Microstructures on Permeability: 3-D Printing Investigation.” *Geophysical Research Letters* 43(14): 7494–7502.

Hua, Wen et al. 2015. “The Influence of Cyclic Wetting and Drying on the Fracture Toughness of Sandstone.” *International Journal of Rock Mechanics and Mining Sciences* 78: 331–35. http://dx.doi.org/10.1016/j.ijrmms.2015.06.010.

Lake, Larry W, Herbert B Carroll, and Thomas C Wesson. 1991. *Reservoir Characterization II*.

Lan, Qing, Hassan Dehghanpour, James Wood, and Hamed Sanei. 2015. “Wettability of the Montney Tight Gas Formation.” In *SPE Unconventional Resources Conference*,.

Li, Guangyu, Xiaoqian Chen, and Yiyong Huang. 2015. “Contact Angle Determined by Spontaneous Imbibition in Porous Media: Experiment and Theory.” *Journal of Dispersion Science and Technology* 36(February): 772–77. http://www.tandfonline.com/doi/abs/10.1080/01932691.2014.921627.

Lozano, Rodrigo et al. 2015. “3D Printing of Layered Brain-like Structures Using Peptide Modified Gellan Gum Substrates.” *Biomaterials* 67: 264–73. http://dx.doi.org/10.1016/j.biomaterials.2015.07.022.

Lucia, F.J. 2007. “Chapter 1 Petrophysical Rock Properties.” In *Carbonate Reservoir Characterization An Integrated Approach*, , 1–27.

M-Flex. 2015. *Particle Size Distribution - Sieve Analysis*.

McKillip William, J. 1989. “Chemistry of Furan Polymers.” *Adhesives from Renewable Resources*: 408–23. http://dx.doi.org/10.1021/bk-1989-0385.ch029.

Mironov, Vladimir et al. 2003. “Organ Printing: Computer-Aided Jet-Based 3D Tissue Engineering.” *Trends in Biotechnology* 21(4): 157–61.

Optima, The V C A, and Optima Xe. 2016. “V CA Optima.”

Osinga, S, G. Zambrano-Narvaez, and R.J Chalaturnyk. 2015. “Study of Geomechanical Properties of 3D Printed Sandstone Analogue.” *American Rock Mechanics Association* 49: 15–547.

Otten, W. et al. 2012. “Combining X-Ray CT and 3D Printing Technology to Produce Microcosms with Replicable, Complex Pore Geometries.” *Soil Biology and Biochemistry* 51: 53–55. http://dx.doi.org/10.1016/j.soilbio.2012.04.008.

Ozbolat, Ibrahim T., and Yin Yu. 2013. “Bioprinting toward Organ Fabrication: Challenges and Future Trends.” *IEEE Transactions on Biomedical Engineering* 60(3): 691–99.

Panda, M N, and L W Lake. 1995. “A Physical Model of Cementation and Its Effects on Single Phase Permeability.” *AAPG Bulletin* 79(3): 431–43.

Primkulov, Bauyrzhan, Jonathan Chalaturnyk, Richard Chalaturnyk, and Gonzalo Zambrano Narvaez. 2017. “3D Printed Sandstone Strength: Curing of Furfuryl Alcohol Resin-Based Sandstones.” *3D Printing and Additive Manufacturing* 4(3): 149–55.

Purcell, W.R. 1949. “Capillary Pressures - Their Measurement Using Mercury and the Calculation of Permeability Therefrom.” *Journal of Petroleum Technology* 1(2): 1949.

Rankin, Timothy M. et al. 2014. “Three-Dimensional Printing Surgical Instruments: Are We There Yet?” *Journal of Surgical Research* 189(2): 193–97. http://dx.doi.org/10.1016/j.jss.2014.02.020.

Revil, André, Pauline Kessouri, and Carlos Torres-Verdín. 2014. "Electrical Conductivity, Induced Polarization, and Permeability of the Fontainebleau Sandstone." *Geophysics* 79(5): D301–18. http://geophysics.geoscienceworld.org/content/79/5/D301.abstract.

Ringrose, P S, and P W M Corbett. 1994. "Controls on Two-Phase Fluid Flow in Heterogeneous Sandstones." *Geological Society, London, Special Publications* 78(1): 141–50. http://sp.lyellcollection.org/content/78/1/141.abstract.

Salathiel, R A. 1973. "Oil Recovery by Surface Film Drainage In Mixed-Wettability Rocks." *Journal of Petroleum Technology*: 1216–24.

Schechter, D. S., D. Zhou, and F. M. Orr. 1994. "Low IFT Drainage and Imbibition." *Journal of Petroleum Science and Engineering* 11(4): 283–300.

Schmitt, C. R. 1974. "Polyfurfuryl Alcohol Resins." *Polymer-Plastics Technology and Engineering* 3(2): 121–58. http://www.tandfonline.com/doi/abs/10.1080/03602557408545025.

Schubert, Carl, Mark C van Langeveld, and Larry A Donoso. 2014. "Innovations in 3D Printing: A 3D Overview from Optics to Organs." *British Journal of Ophthalmology* 98(2): 159–61. http://bjo.bmj.com/lookup/doi/10.1136/bjophthalmol-2013-304446.

Selvadurai, A. P S, and A. Głowacki. 2008. "Permeability Hysterisis of Limestone during Isotropic Compression." *Ground Water* 46(1): 113–19.

De Silva, G. P D, P. G. Ranjith, M. S A Perera, and B. Chen. 2016. "Effect of Bedding Planes, Their Orientation and Clay Depositions on Effective Re-Injection of Produced Brine into Clay Rich Deep Sandstone Formations: Implications for Deep Earth Energy Extraction." *Applied Energy* 161: 24–40. http://dx.doi.org/10.1016/j.apenergy.2015.09.079.

De Silva, G.P., M.S.A. Perera, and P.G. Ranjith. 2014. "The Effect of Layer Pattern on Flow Properties through Deep Reservoir Rocks." *ISRM International Symposium - 8th Asian Rock Mechanics Symposium, ARMS 2014* (October): 2671–79.

Unsal, E., G. Mason, N. R. Morrow, and D. W. Ruth. 2007. "Co-Current and Counter-Current Imbibition in Independent Tubes of Non-Axisymmetric Geometry." *Journal of Colloid*

and Interface Science 306(1): 105–17.

Ventola, C Lee. 2014. "Medical Applications for 3D Printing: Current and Projected Uses." *journal for formulary management* 39(10): 704–11. http://www.ncbi.nlm.nih.gov/pubmed/25336867%0Ahttp://www.pubmedcentral.nih.gov/articlerender.fcgi?artid=PMC4189697%0Ahttp://www.pubmedcentral.nih.gov/articlerender.fcgi?artid=4189697&tool=pmcentrez&rendertype=abstract.

Wang, Zhi, Atac Tuli, and William A Jury. 2003. "Unstable Flow during Redistribution in Homogeneous Soil." *Vadose Zone Journal* 2: 52–60.

Wardlaw, N. C., and R. P. Taylor. 1976. "Mercury Capillary Pressure Curves and the Interpretation of Pore Structure and Capillary Behaviour in Reservoir Rocks." *Bulletin of Canadian Petroleum Geology* 24(2): 225–62.

Washburn, E. W. 1921. "Note on a Method of Determining the Distribution of Pore Sizes in a Porous Material." *Proceedings of the National Academy of Sciences of the United States of America* 7(4): 115–16.

Wei, Mike, Robert Bowman, John L. Wilson, and Norman R. Morrow. 1993. "Wetting Properties and Stability of Siliane-Treated Glass Exposed to Water, Air and Oil." *Journal of Colloid and Interface Science* 157: 154–59.

Yassin, Mahmood Reza, Hassan Dehghanpour, James Wood, and Qing Lan. 2016. "A Theory for Relative Permeability of Unconventional Rocks With Dual-Wettability Pore Network." In *Unconventional Resources Technology Conference*, , 1–11.

Zimmerman, R.W. 1991. *Compressibility of Sandstones*.